FACULDADE DE ENGENHARIA DA UNIVERSIDADE DO PORTO

Biomechanical Study of Autologous Graft Characteristics and Surgical Techniques in Anterior Cruciate Ligament Reconstruction

Filipa Rodrigues Pato

Master in Bioengineering - Biomedical Engineering

Supervisors: Prof. Dr. António Torres Marques,

Prof. Dr. António Manuel Ramos

July 31, 2026

Resumo

A reconstrução do ligamento cruzado anterior (LCA) é um dos procedimentos ortopédicos mais frequentemente realizados, permanecendo, ainda assim, com taxas de falha reportadas na literatura consideráveis. A seleção do enxerto é habitualmente orientada pela ideia de mimetizar a rigidez global do enxerto à do ligamento nativo, niglegenciando uma discrepância morfológica fundamental: o LCA apresenta uma área de secção transversal variável, enquanto os enxertos convencionais são preparados como estruturas cilíndricas de secção constante. Esta dissertação recorre à modelação por elementos finitos para avaliar de que forma a rigidez e esta transição geométrica influenciam a biomecância do joelho.

Foi desenvolvido num modelo tridimensional da articulação do joelho, em SolidWorks, um LCA geometricamente calibrado a partir de valores de secção transversal reportados na literatura. Foi aplicada, em todas as simulações, uma carga tibial anterior padronizada de 134 N. Numa primeira fase, o módulo de elasticidade do ligamento nativo foi variado (199, 320 e 465 MPa, representando condições laxa, normal e rígida). Numa segunda fase, o ligamento nativo foi substituido por um enxerto cílindrico fixado no topo dos túneis femoral e tibial, com propriedades representativas dos três enxertos autólogos mais comuns: osso-tendão patelar-osso (E = 597 MPa), tendão quadricipital (E = 312 MPa) e tendão isquiotibial (E = 154 MPa).

O aumento da rigidez do ligamento nativo reduziu de forma consistente o deslocamento tibial anterior e a deformação intraligamentar, ao mesmo tempo que aumentou a tensão de von Mises interna, sem alterar a localização do seu pico a seguir à inserção femoral, a secção transversal mais estreita do ligamento. As forças resultantes nas inserções, contudo, variaram de forma não monótona com a rigidez, atingindo os valores mais baixos na condição normal. Na fase de reconstrução, o deslocamento seguiu a mesma relação inversa com a rigidez do enxerto, mas foi consideravelmente superior ao observado em qualquer cenário nativo, apesar do módulo de elasticidade superior do BPTB, uma discrepância atribuída à maior complacência introduzida pela fixação nos túneis ósseos e a outros fatores específicos do modelo, e não apenas às propriedades do material. As concentrações de tensão e deformação também se deslocaram da inserção do ligamento para as entradas dos túneis ósseos: enxertos mais rígidos desenvolveram maior tensão intra-enxerto mas menor tensão na interface, enquanto enxertos mais flexíveis revelaram o padrão inverso, evidenciando um compromisso entre a exigência interna do enxerto e a carga nos túneis. O tendão quadricipital ocupou uma posição intermédia em praticamente todos os parâmetros avaliados.

Estes resultados indicam que equiparar a rigidez global de um enxerto à do LCA nativo é insuficiente para reproduzir o seu comportamento biomecânico. A transição para uma secção transversal constante, em conjunto com as diferenças nas condições de inserção e fixação, redistribui a tensão e a deformação internas em direção às entradas dos túneis ósseos, identificando esta região, e não apenas a escolha do material do enxerto, como o principal local de vulnerabilidade estrutural na reconstrução do LCA.

Palavras-chave: Ligamento Cruzado Anterior; Reconstrução do LCA; Análise por Elementos Finitos; Rigidez; Biomecânica de Enxertos Autólogos

Abstract

Anterior cruciate ligament (ACL) reconstruction is one of the most frequently performed orthopaedic procedures, yet reported failure rates remain considerable. Graft selection typically matches the global stiffness of the autograft to the native ligament, overlooking a key morphological discrepancy: the ACL has a variable, non-uniform cross-sectional area, whereas conventional autografts are prepared as constant-section cylinders. This dissertation uses finite element modelling to evaluate how stiffness and this geometric transition affect knee biomechanics.

A three-dimensional model of the knee joint incorporating a native ACL geometry, calibrated with cross-sectional values reported in literature, was developed. A standardized 134 N anterior tibial load was applied throughout. In a first phase, the native ligament's Young's Modulus was varied (199, 320, and 465 MPa, representing lax, normal, and stiffened conditions) to assess its effect on anterior tibial displacement, internal stress and strain, and resultant insertion forces. In a second phase, the native ligament was replaced by a cylindrical graft anchored within femoral and tibial bone tunnels, with material properties representative of the three most common autografts: bone-patellar tendon-bone (BPTB, E = 597 MPa), quadriceps tendon (QT, E = 312 MPa), and hamstring tendon (HT, E = 154 MPa).

Increasing native ligament stiffness consistently reduced anterior tibial displacement and intra-ligamentous strain (from 3,75% to 2,25%), while increasing internal von Mises stress (from 9,0 to 13,2 MPa), consistently concentrated at the femoral insertion, the ligament's narrowest cross-section. Insertion forces, however, varied non-monotonically with stiffness, reaching their lowest values under the normal condition. In reconstruction, displacement followed the same inverse relationship with graft stiffness, but was substantially greater than under any native scenario, despite even higher Young's Modulus, a discrepancy attributed to compliance introduced by the tunnel-anchored fixation and other model-specific factors rather than material properties alone. Stress and strain concentrations also relocated from the ligament insertion to the bone tunnel apertures: stiffer grafts developed higher intra-graft stress but lower interface stress, while more compliant grafts showed the inverse pattern, revealing a trade-off between internal graft demand and tunnel loading. The quadriceps tendon graft occupied an intermediate position across nearly all parameters.

These results indicate that matching the global stiffness of a graft to the native ACL is insufficient to reproduce its local biomechanical behavior. The transition to a constant cross-section, together with differences in insertion and fixation conditions, redistributes internal stress and strain toward the bone tunnel apertures, identifying this region, rather than graft material alone, as the principal site of structural vulnerability in ACL reconstruction.

Keywords: Anterior Cruciate Ligament; ACL Reconstruction; Finite Element Analysis; Stiffness; Autograft Biomechanics

UN Sustainable Development Goals

The Sustainable Development Goals (SDGs) , established by the United Nations, address the environmental, social, and economic dimensions of sustainability [1]. Biomedical engineering, as a discipline that applies engineering principles to clinical problems, plays a recognized role in advancing these goals, particularly in promoting health and developing evidence-based technological solutions. This dissertation, focused on the computational biomechanical study of autologous grafts and surgical techniques in ACLR, contributes to SDG 3 (Good Health and Well-Being), SDG 4 (Quality Education) and SDG 9 (Industry, Innovation and Infrastructure).

Table 1 identifies the SDG's metrics to which this work makes justifiable contributions, specifying the relevant targets and associated performance indicators.

The contributions identified are presented conscientiously: this dissertation alone cannot resolve the challenges associated with the SDGs, but constitutes a measurable scientific contribution to their progress. The work aims to advance evidence-based orthopaedic practice (SDG 3), supports postgraduate research training in biomedical engineering (SGD 4), and develops an innovative finite element framework embedded within a competitively funded Portugues research project (SDG 9). Together, these contributions reflect part of the role of biomedical engineering as a driver of sustainable development, reinforcing the alignment between scientific research and the goals of the United Nations 2030 Agenda.

Table 1: Synthesis of how the present work contributes for SDG.

SDG	Goal	Contribution	Performance indicators and metrics
3	**3.4 Non-communicable diseases and mental health**	Reducing graft failure rates and improve surgical clinical outcomes in ACLR. Comparing the mechanical behavior of autologous graft against the native ACL, provide a scientific evidence base for more informed graft selection, contributing to the reduction of musculoskeletal morbidity and the promotion of patient well-being.	Graft failure rate in ACLR. Contribution to evidence based surgical protocols.
	3.8 Universal health coverage	The development of predictive computational models of post-reconstruction knee biomechanics can, in the longer term, support surgical simulation systems and personalised pre-operative planning tools, contributing to equitable access to high-quality orthopaedic care.	Applicability across diverse patient populations through model parametrisation (geometry, graft stiffness).
4	**4.b Higher education scholarships and capacity**	The framework of the ACLART research project (Project No. 15022), contributes to the training of researchers in advanced computational biomechanics and biomedical engineering. Promotes the development of specialized scientific competencies at postgraduate level.	Completion of a Master's degree in Biomedical Engineering at FEUP. Contribution to the ACLART research project's knowledge base. Development of advanced skills in finite element modelling, biomechanical analysis, and scientific writing.
9	**9.5 Research and innovation upgrade**	Replacing empirical assumptions with a data-driven approach. The parametric analysis of stiffness, material non-linearity, and graft geometry represents a contribution to bioengineering research. It is inserted within the ACLART project (No. 15022), co-financed by ERDF under the Portugal 2030 program and the Foundation for Science and Technology (FCT).	Development of a validated, parametrisable FEM model. Academic dissemination of results. Contribution to a competitively funded Portuguese research project.

Acknowledgment

Nos últimos meses falei deste projeto com entusiasmo, desespero, e tudo o que existe entre os dois. Esta página é para todos os que escolheram ficar, e ouvir.

Antes de mais, à equipa de orientação que tornou possível este trabalho. Ao Prof. Dr. António Torres Marques pela partilha de conhecimento, ao Prof. Dr. José Simões pelo espírito crítico, ao Prof. Dr. António Ramos pela paciência, e aos três pela disponibilidade e simpatia que tornaram este percurso um pouco mais leve. Estendo também o meu agradecimento ao Dr. Orlando Simões por ter possibilitado que visse de perto o procedimento cirúrgico abordado e ao Projeto n.º 15022 (ACLART – Previsão de Resultados Clínicos da Reconstrução do Ligamento Cruzado Anterior através de Simulação In Silico Combinada com Inteligência Artificial), referência COMPETE2023-FEDER-00867200, cofinanciado pelo Fundo Europeu de Desenvolvimento Regional (FEDER) no âmbito do programa PORTUGAL2030 e pela Fundação para a Ciência e a Tecnologia, I.P. (FCT), sob o qual se realizou esta Dissertação.

À minha família, por serem o meu pilar fundamental e pelas bolachas de baunilha que melhoraram tantos dos meus dias. Em especial, aos meus pais, por me permitirem fazer casa de uma cidade que não é a deles sem alguma vez sentir que estão longe, por confiarem em mim, por não terem medo de me ver falhar e por não só me deixarem voar, como me incentivarem a fazê-lo. Inês, por seres a minha maior certeza e o meu maior exemplo, e pelo rato rosa que me acompanhou estes meses. Dé e Bia, por cumprirem comigo um sonho de pequenina. A todos, obrigada por me mostrarem o que é verdadeiramente importante e por me fazerem ter orgulho em quem sou e de onde vim.

Aos que nos últimos 5 anos fizeram da FEUP a minha casa: aos que estavam quando cheguei, aos que ficam agora que vou e especialmente aos que chegaram e vão (ou não) comigo. A estes últimos, de 021, obrigada por serem os meus melhores amigos sem que eu percebesse quando aconteceu. Pelo dia a dia que transformaram em algo divertido, emocionante e feliz, e por me provarem que a rotina, quando é com as pessoas certas, não cansa. Não escolhia partilhar esta viagem com mais ninguém, e enche-me de orgulho saber que chegamos separados mas vamos juntos.

Do outro lado da rua, à AEFEUP, por me ter dado o privilégio de viver tanto. Aos 6 que ao longo deste ano acreditaram na minha capacidade de conciliação, por me mostrarem que não precisamos sempre de concordar para construir algo bonito e por me apoiarem sempre com uma palavra amiga ou mesmo com o SolidWorks. Ao Desportivo, por fazerem acontecer, por me tornarem uma versão melhor de mim mesma e por nunca deixarem que o poder me subisse à cabeça. À AEFEUP, e ao Desportivo no coração, sempre.

Àquelas que partilharam o campo comigo, de todas as cores, obrigada por serem o fim de dia que, mais que uma obrigação, me apetecia ter. Por me fazerem sentir que vale a pena, e por me mostrarem que o desporto tem uma forma muito particular de unir pessoas, e eu tive a sorte de descobrir isso convosco.

Por fim, às duas estrelas mais brilhantes, que nunca deixaram de ser inspiração e exemplo.

"Aqueles que passam por nós não vão sós. Deixam um pouco de si, levam um pouco de nós." Obrigada por me deixarem levar um pouco de todos vocês.

Que comece o resto da vida,

Filipa Pato

"Just keep swimming."

Dory

Contents

List of Figures

List of Tables

Nomenclature

ACL	Anterior Cruciate Ligament
ACLR	Anterior Cruciate Ligament Reconstruction
AM	Anteromedial
BMI	Body Mass Index
BPTB	Bone-Patellar Tendon-Bone
CAD	Computer-Aided Design
CSA	Cross-Sectional Area
CT	Computational Tomography
DoF	Degree of Freedom
G4	Quadrupled Gracilis
GST4	Quadrupled Semitendinosus-Gracilis
HT	Hamstring Tendon
K	Stiffness
LCL	Lateral Collateral Ligament
MCL	Medial Collateral Ligament
MRI	Medical Resonance Image
PCL	Posterior Cruciate Ligament
PL	Posterolateral
PT	Patellar Tendon
QT	Quadriceps Tendon
SDGs	Sustainable Development Goals
ST3	Tripled Semitendinosus
ST4	Quadrupled Semitendinosus

Chapter 1

Introduction

1.1 Context and Motivation

Anterior Cruciate Ligament (ACL) reconstruction (ACLR) is one of the most frequently performed orthopedic procedures globally, essential for restoring knee stability in active individuals and athletes after the rupture of the native ligament [2].

Despite ongoing research and advancements in treatment of ACL injuries over the past few decades, the goal of restoring knee function and preserving long-term knee-related health remains a challenge [3]. A large meta-analysis, performed in 2017, using 47 613 knees as study object, presented a failure rate around 2,8% [4], while other works refer the same rate to be from 6% to 20% [5, 6, 7, 8, 9]. Although reported failure rates vary significantly across clinical cohorts, the consensus in current literature remains that a considerable percentage of patients will experience graft rupture after a primary ACLR.

The reasons for a primary ACLR failure can be broadly sub-grouped into traumatic re-injury, technical issues, and biological failure. Failures stemming from technical errors constitute the highest proportion, 77% to 95% for Elfekky et al. [5] or 64,5% for Tapasvi and Shekhar [10], causing instability. Within technical errors, non-anatomical inaccurate femoral and tibial tunnel placement is recognized as the most frequent and critical cause, accounting for 70% to 85% ([5, 10]) of all such technical issues. Other strong correlations found between non-traumatic technical failure were with transtibial femoral drilling technique, and use of femoral trans-fixation devices [10]. Biological failure, meanwhile, is typically attributed to disturbances in revascularization, inhibited cellular proliferation, or difficulty in the ligamentization process, leading to lack of graft incorporation or necrosis. Infection rate after ACLR is very low but is also an important cause of failure of reconstruction [5, 10]. This persistent rate of failure, dominated by technical and positioning errors, underscores the necessity for rigorous biomechanical analysis and procedural refinement.

Beyond catastrophic graft failure, clinical success is multifaceted and must be evaluated through patient-reported instability, joint laxity, and objective functional measures. Parameters such as donor-site morbidity, muscle strength deficits, and long-term joint flexibility are equally critical to the patient's quality of life [3, 11]. Achieving these optimal outcomes requires a precise synergy between multiple biomechanical factors, from graft selection and anatomical tunnel placement to tensioning and secure fixation [7]. Given the ACL's fundamental role in constraining translational and rotational forces, it is imperative that surgeons base graft choices on a deep understanding of the biomechanical implications inherent to each tissue type [12].

The core of the current clinical challenge resides in the immense variability of treatment options, ranging from autografts and allografts to emerging synthetic solutions, and the inherent difficulty in predicting their *in vivo* mechanical performance. Often, surgical decisions are guided by surgeon preference or limited clinical evidence rather than a comprehensive assessment of the biomechanical properties of the entire 'graft-fixation-joint' complex [5, 12].

This work aims to be another step towards the creation of a fully comprehensive framework in ACLR. The goal is to establish a comparative biomechanical profile between the complex, non-uniform morphology of the native ACL [13] and the simplified, cylindrical geometries typical of conventional surgical grafts. Additionally, this investigation incorporates a parametric evaluation of tissue stiffness to determine how variations in the ligament's material properties interact with these geometric configurations to influence overall joint stability.

Therefore, the primary objective of this study is to investigate how this transition from a variable native cross-section to a constant graft geometry alters the internal stress distribution and localized joint kinematics under standardized clinical loads. By isolating and cross-analyzing the structural influence of shape and the functional impact of material stiffness, this computational framework seeks to replace empirical grafting assumptions with a data-driven strategy, ultimately providing a deeper predictive understanding of graft performance and its long-term biomechanical integration.

1.2 Document Structure

This document is organized into chapters.

Chapter 1 is the current chapter and contains a brief introduction to the study.

Chapter 2 presents the literature review and state of the art in ACLR. It is divided into four distinct sections that address the anatomy of the knee, the problem of ligament rupture, its characterization and reconstruction, a review of the current graft solutions and their morphological and biomechanical definition, and some computational and experimental studies on the subject.

Chapter 3 describes the methodology adopted to develop the computational model of the knee for the practical work and its specificities.

Chapter 4 contains the analysis and discussion of results. It addresses the biomechanical outputs of the simulated joint configurations, providing a direct comparative analysis between the baseline native conditions, under varying stiffness and non-linear material behavior, and the post-reconstruction scenarios utilizing Bone-Patellar Tendon-Bone (BPTB), Hamstring Tendon (HT), and Quadiceps Tendon (QT) grafts. The localized stress distributions, equivalent strain patterns, and anterior tibial translations are evaluated and discussed in light of current clinical and orthopedic literature.

Finally, Chapter 5 presents the conclusions of the study, its limitations, and proposes possible future research.

Chapter 2

Literature Review

2.1 Knee's Anatomy

The human body is often described as the most complex machine, comprised of approximately 206 bones that articulate at various joints. Among these, the knee (Figure 2.1) is frequently regarded as the most structurally complex joint in the human musculoskeletal system because it must simultaneously ensure high stability, bear the body's mass, and maintain load-bearing capacity while being subjected to diverse and high physiological stresses, all while facilitating the critical movements of extension, flexion, and a small degree of leg rotation [14, 15, 16].

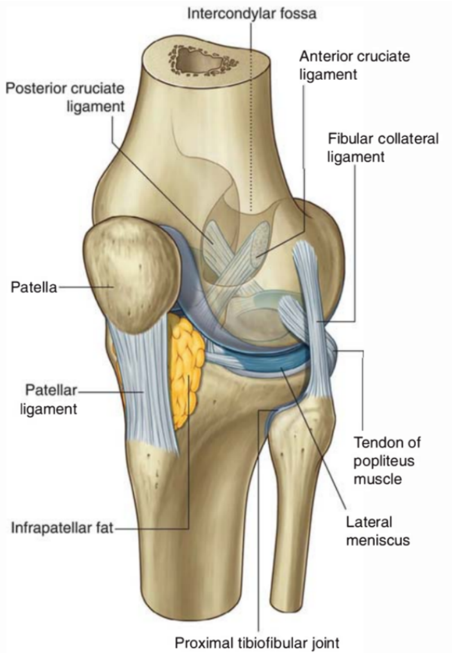

Figure 2.1: Knee joint. Joint capsule is not shown. [17]

The knee is a synovial joint, meaning it establishes a connection between two bony extremities. It is composed of articular cartilage, ligaments, synovial fluid, and an articular capsule, encompassing three bones: the femur (the longest bone in the human body), the tibia, and the patella. Together, these structures form two distinct articulations: the tibiofemoral and the femoropatellar joints [14, 17, 18].

The tibiofemoral joint, which ensures the support of body mass, is established by the articulation of the distal end of the femur (the femoral condyles) and the proximal end of the tibia (the tibial plateaus). The medial femoral condyle, which is larger and has a higher radius of curvature than the lateral condyle, interacts with the medial tibial plateau, which possesses an oval and concave shape. Conversely, the lateral condyle interacts with the lateral tibial plateau, characterized by a circular and convex geometry. This interaction contributes to the alignment and stability of the knee, allowing femoral rotation over the tibia across three axes and limited anteroposterior femoral translation [14, 16, 18].

On the other hand, the femoropatellar joint realizes the interaction between the largest sesamoid bone, the patella, and the anterodistal femoral groove. Located between the tibia and the femur, the patella is embedded within the quadriceps tendon, covering and protecting the anterior articular surface of the knee. In addition to providing a larger area for the distribution of compressive stresses on the femur, resulting from the increased contact area between the two bones, this structure is crucial for joint stability. It provides a significant mechanical advantage to the knee extension mechanism, reducing the force required by the quadriceps muscles to extend the knee by 15% to 30% [14, 18].

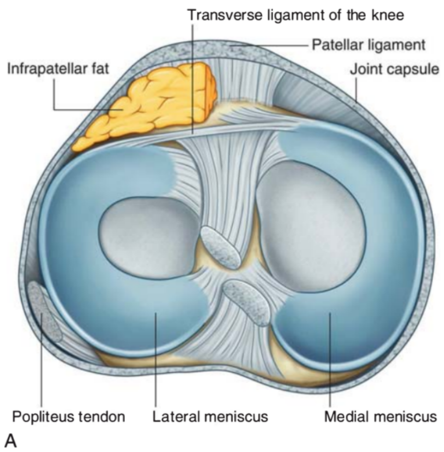

Figure 2.2: Menisci of the knee joint (superior view) [17].

With their unique laminar structure and crescent-shaped geometry, the menisci (Figure 2.2) are fibrocartilaginous and fibroelastic structures located between the femoral condyles and the tibia. These soft tissues present specific geometries on their surfaces, concave superiorly and flat inferiorly, to ensure the respective interfaces with the femoral condyles and tibial plateaus [19]. In this way, the menisci ensure the stability and damping of the knee joint, performing a wide range of biomechanical functions, such as optimizing axial load transmission and minimizing contact pressure peaks on the cartilage; their elasticity also allows them to act as shock absorbers. For both menisci, the inferior surface is not entirely anchored to the tibial plateaus and they connect to the femoral condyles through meniscofemoral ligaments, which support and facilitate their biomechanics. However, the medial meniscus is wider and thinner than the lateral meniscus, covering between 50% and 60% of the medial tibial plateau. At a mechanical level, the medial meniscus contributes primarily to control anteroposterior translation, while the lateral meniscus helps resist joint rotation [14, 18].

Articular cartilage, which is avascular and aneural, is characterized as a porous tissue with viscoelastic behavior. It coats the ends of the joint's bony structures, promoting low-friction gliding due to its chemical composition based on fibrous collagen networks and high-water content. The presence of cartilage significantly reduces contact forces within the knee, mitigating impact shock [14, 16].

To ensure joint stability and prevent excessive translation, rotation, and angulation (valgus or varus) of the leg, there are ligaments, structures composed of parallel and densely packed collagen fibers that establish relationships between bones. These insert directly into the bone via fibrocartilage and mineralized fibrocartilage or indirectly through superficial fibers connected to the periosteum and deeper fibers attached directly to the bone at acute angles [16, 18]. There are four primary ligaments, illustrated in Figure 2.3, uniting the femur and the tibia: two collateral ligaments, the lateral (LCL) and medial (MCL), which stabilize the knee mediolaterally, in the coronal plane, and two intra-articular and extrasynovial ligaments that control knee movement anteroposteriorly, in the sagittal plane: the anterior cruciate ligament and the posterior cruciate ligament (PCL) [15, 16].

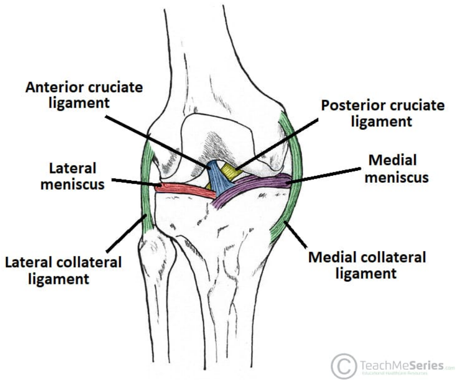

Figure 2.3: Ligaments of the knee joint [20].

Beyond the isolated analysis of the morphological properties of each ligament, understanding the knee as a functional unit requires an evaluation of its integrated biomechanics. Joint stability resides in the interdependence between these structures, as the failure of one element drastically alters the load distribution across the others. An injury to the MCL, whose primary function is to restrict valgus rotation, causes an increase in the loads borne by the ACL; therefore, the probability of an ACL injury increases considerably when an MCL injury exists in the same knee. Although less frequent, injuries to the LCL, responsible for limiting varus rotation, can also occur. These can be more incapacitating than MCL injuries due to the high loads the LCL is subjected to during the gait cycle. Additionally, this type of injury is commonly associated with cruciate ligament injuries, as LCL laxity promotes a higher concentration of loads on these ligaments. Thus, in cases of cruciate ligament injuries, the reconstruction of the lateral collateral ligament is also suggested to reduce the probability of failure in the cruciate ligament reconstruction. The PCL is located in the medial compartment of the knee joint and is considered the strongest and largest of the intra-articular ligaments. The PCL provides the necessary rotational stability in anteroposterior movement. Nevertheless, this ligament cannot resist anterior displacement, as the ACL is the primary restrictor of anterior tibial translation. Although less common than ACL injuries, a PCL injury results in considerable joint instability, with its greatest effect occurring at 90° of knee flexion [14, 16].

2.1.1 Anterior Cruciate Ligament

The ACL is the primary stabilizer of anterior tibial translation relative to the femur, ensuring approximately 90% of the resistance to such movement between 30º and 90º of flexion. Additionally, it acts to restrict internal rotation and, to a lesser extent, external rotation, valgus and varus deformation during knee extension, and hyperextension [14, 16, 18]. It is located in the central compartment of the knee joint, connecting the medial face of the lateral femoral condyle to the anterior area of the tibia. Despite being intracapsular, it is considered extra-synovial, as it is enveloped by a synovial membrane that isolates it from the joint fluid [15, 16, 18].

The femoral insertion has an approximately vertical orientation and is located in the posterior portion of the medial face of the lateral femoral condyle. The tibial insertion, with an approximately transverse orientation, is found in a fossa located anterior and external to the anterior tibial spine [15, 16]. The shape of the tibial insertion is oval, measuring approximately 18 mm in anteroposterior length and 11 mm in width, whereas the femoral insertion is smaller, with a length of 17 mm and a width of 10 mm. Among the ligamentous structures, the ACL is the only one without any capsular insertion [16]. Spatially, the ACL follows an anterior, medial, and distal orientation from the femoral to the tibial insertion; due to the orientation of these footprints, an external torsion of the ACL fascicles occurs [15]. Some studies suggest that the tibial and femoral insertion areas range between 114 mm^2 and 229 mm^2 and between 83 mm^2 and 197 mm^2, respectively [18]. However, Kopf et al. [21] demonstrates through an extensive literature review that insertion site dimensions vary even more drastically across different scientific reports, with several studies showcasing values well outside these conventional ranges. This high dispersion highlights that there is no consensus on a single standard size, making deviations from specific intervals both common and methodologically acceptable.

Morphologically, the ACL does not possess a uniform cylindrical shape. Instead, it exhibits a complex, non-constant cross-sectional area (CSA) along its length. The ligament is notably wider at its attachment sites and tapers toward a narrower mid-substance. This geometric variability is functionally significant, as it influences stress distribution and fiber recruitment patterns during joint loading [13]. According to Fernandes [22], the CSA varies significantly at different levels of the ligament, with reported values of 34 mm^2 near the femoral insertion, 35 mm^2 at the mid-substance, and 42 mm^2 immediately before tibial insertion (see Figure 2.4). This anatomical complexity contrasts with the constant cross-sections typically found in surgical grafts, representing a critical factor in the biomechanical fidelity of ACL reconstructions.

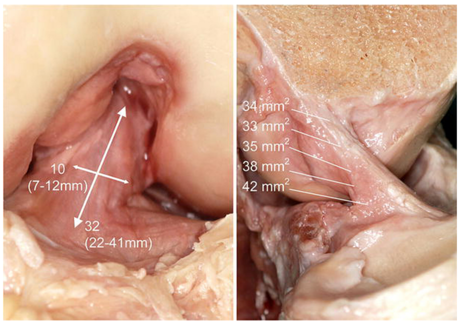

Figure 2.4: Size and variation of the LCA CSA [22].

The ACL is a band of connective tissue composed of two functional bundles: the anteromedial (AM) bundle, which originates at the most proximal portion of the lateral femoral condyle and inserts at the most anteromedial portion of its tibial footprint, and the posterolateral (PL) bundle, which originates more posteriorly and distally at the femoral insertion and attaches more postero-laterally on the tibia [14, 15, 16, 18]. The tension of the collagen fibers constituting these two bundles varies throughout the knee movement. In extension, as shown in Figure 2.5, the femoral attachment of the ACL is in a vertical position and the fibers are parallel, with the PL bundle fibers slightly more tensioned than those of the AM bundle. Conversely, during flexion, the AM bundle's femoral insertion site rotates posteriorly and inferiorly, in contrast to the PL bundle's femoral insertion, which rotates anteriorly and superiorly, maintaining the AM bundle taut while the PL bundle becomes more relaxed [15, 21]. If hyperextension occurs, tension is further accentuated due to impingement with the intercondylar notch [15]. Morphologically, studies indicate that the AM bundle is longer than the PL bundle, but as a whole, the ACL has a length of approximately 30 mm [18, 21, 23]. Regarding the angle formed between the sagittal plane of the joint and the body of the ACL, it lies between 12° and 37° in the coronal projection. Furthermore, the ligament describes an average angle of 25° projected in the sagittal plane, relative to the plane parallel and coincident with the tibial plateau (transverse plane) [18].

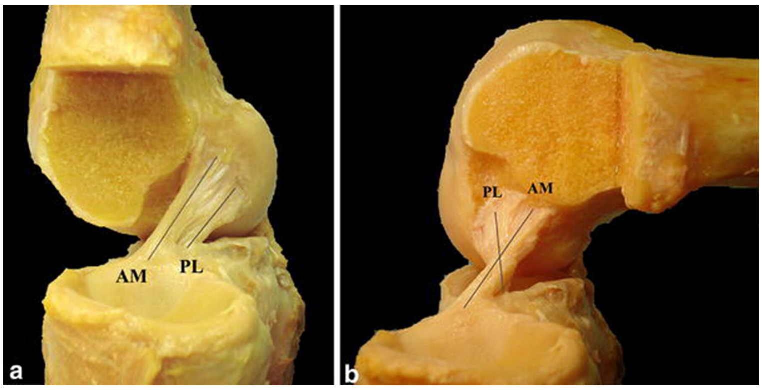

Figure 2.5: Extended knee with an almost vertical femoral ACL origin and parallel AM and PL bundles (a), and a 90° flexed knee with an almost horizontal ACL origin and twisted AM and PL bundles (b) [21].

The blood supply of both cruciate ligaments depends on the middle genicular artery, which vascularizes the surrounding synovium. Vascularization is also promoted by Hoffa's fat pad, but the blood supply to the ACL is generally considered poor. This, in turn, contributes to the ACL's limited capacity for healing. Innervation is maintained by mechanoreceptors from the popliteal plexus (originating primarily from the posterior articular branch of the posterior tibial nerve), which are fundamental for proprioception. The minimal presence of nociceptors explains the low intensity of pain immediately following an acute rupture, prior to the development of painful hemarthrosis. Some studies point to the existence of a vascularized connective tissue septum located between the AM and PL bundles, which serves to separate them [15, 24, 25].

2.2 ACL Rupture

2.2.1 Injury Mechanisms and Characterization

ACL injuries occur most frequently during sports activities, accounting for approximately 70% of ruptures, and can be classified as either contact or non-contact injuries. The former occurs when an external force is applied to the knee in addition to the ground reaction force, while the latter, representing nearly 70% of all ACL ruptures, occurs during motor actions where the ground reaction force is the only external agent [15, 16]. Beyond factors such as age, sex, body mass index (BMI), and sports activity level, anatomical factors such as notch stenosis, constitutional hyperlaxity, or intrinsic ACL weakness may also increase an individual's susceptibility to injury [16].

These injuries are often the result of low-velocity trauma or deceleration combined with a rotational component, typically associated with sudden changes in direction or unconventional falls [16].

The most frequent injury mechanism, represented in Figure 2.6, consists of a combination of slight flexion and a varus angle of the leg with external, medio-lateral, rotation of the femur, generating high tension in the ACL and generally resulting in an isolated rupture of the AM bundle [18]. This situation often leads to injuries of the mid-portion of the lateral capsule and, occasionally, bony avulsions known as Segond fractures [16]. More rarely, the ACL may rupture through a combination of slight flexion and a valgus angle with internal (latero-medial) rotation of the femur [15, 26]. These mechanisms are primarily associated with sudden changes in direction while running or abrupt variations in speed [18].

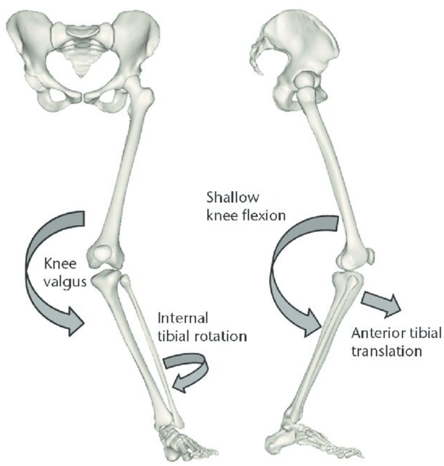

Figure 2.6: Most common biomechanical injury mechanisms. Flexion, valgus, internal rotation (left). Flexion, varus, external rotation (right) [27].

Furthermore, the biomechanical role of the quadriceps muscle as an ACL antagonist is critical at low flexion angles, those between 0° and 30°. Vigorous quadriceps contraction in these positions generates significant anterior tibial translation, increasing the strain on the ligament fibers and potentially leading to non-contact ruptures [28]. Another injury mechanism can occur during knee hyperextension, where the ligament impinges against the roof of the intercondylar notch, particularly if stenosed, leading to the rupture of the PL bundle and potentially the AM bundle if the stenosis is severe. This is generally associated with jumping maneuvers [18]. It is also important to refer that, associated with ACL ruptures, injuries may also occur in the lateral meniscus suspensory ligaments, the iliotibial band, and avulsions of Gerdy's tubercle [16]. Concomitant injuries to the PCL, MCL, or LCL may also be observed.

ACL injuries are classified into three grades of severity:

- **Grade I:** The ligament is slightly stretched but remains capable of maintaining knee joint stability;
- **Grade II:** The ligament undergoes greater distension, resulting in a partial rupture of fibers in one or both bundles;
- **Grade III:** Complete rupture (both bundles) or nearly complete rupture (one bundle) of the ligament.

Complete or nearly complete ruptures usually disrupt blood flow, so surgical intervention is recommended to reconstruct the ligament, which does not have self-regenerative properties [14, 18].

ACL rupture accentuates anterior tibial translation, primarily due to the advancement of the lateral tibial plateau. The more severe the internal capsulo-ligamentous injury, the greater the anterior translation of both tibial plateaus, caused by the combined ligamentous rupture and damage to internal joint structures. External capsulo-ligamentous injuries further accentuate the mobility of the lateral compartment [16].

2.2.2 Reconstruction - Current Surgical Trends

Although ACL reconstruction has been performed since the beginning of the twentieth century, being one of the most common orthopedic procedure, there is still debate in orthopedic literature about the optimal technique. Timing, graft choice, number of tunnels, tunnel location, fixation techniques, and rehabilitation protocols still continue to be enhanced [29].

The primary goal of ACLR is to preserve joint homeostasis and enable the patient to return to pre-injury activity level. These objectives require restoring the native anatomy, ensuring stable fixation, and re-establishing biomechanical function [21, 29]. The evolution of surgical techniques, driven by an increasing understanding of joint biomechanics and graft quality, encompasses approaches ranging from isolated sutures to combined intra and extra-articular plasties [16, 18, 30]. Isolated sutures preserve the proprioception of the ligament and avoid donor-site morbidity. However, they often yield inconsistent clinical outcomes in mid-substance tears and degrade over time [16, 18, 31]. On the other hand, isolated extra-articular plasties have proven ineffective in the long term and may induce osteoarthritis in the internal compartment [16, 18]. Currently, the literature supports the use of single-bundle intra-articular reconstructions, as double-bundle techniques do not offer biomechanical or clinical advantages that justify the increased cost and surgical complexity [16, 32, 33].

Intra-articular reconstructions generally consist of drilling tunnels in the femur and tibia to fix a tissue graft, aiming for a behavior as similar as possible to the original anatomy. In this context, the stiffness of the complex is one of the primary predictors of success. In these types of surgeries, graft healing in bone tunnels is a complex process influenced by the type of graft used, method of fixation, tunnel placement, graft motion, and tensioning [34].

The geometric optimization of bone tunnels is a determinant factor for the success of ACL reconstruction. According to the studies of Nogueira and Matos [14] and Ramos et al. [35], the ideal inclination for the tibial tunnel is identified as 45° in the sagittal projection (relative to the transverse plane) and 30° in the coronal projection. Regarding the femoral tunnel, the literature suggests that an inclination of 45° in both the coronal and sagittal planes minimizes maximum stress at the tunnel entrance and within the graft itself, significantly reducing the risk of failure and bone tunnel widening [14, 18]. It is widely accepted that the restoration of knee biomechanics is more sensitive to the precise location of the femoral tunnel than to the intrinsic material properties of the graft [14]. In fact, the position of the ligament footprint can influence the maximum load by approximately 20% [35]. This relationship is heavily dictated by the concept of isometry, where tunnel positioning affects the tension and length of the graft during joint movement (Figure 2.7). Specific positioning points illustrate this impact: a tunnel placed too far anteriorly on the femur (red point) results in a drastic increase in the distance between tunnels as the knee flexes (Figure 2.7b), imposing excessive tension that may lead to graft failure or tunnel widening. Conversely, the traditional ideal position (green point) represents the isometric benchmark, where graft length and tension remain relatively constant throughout the range of motion, ensuring joint stability. Finally, a very posterior position (blue point, "over-the-top") leads to increased graft length and tension as the knee is extended (Figure 2.7a).

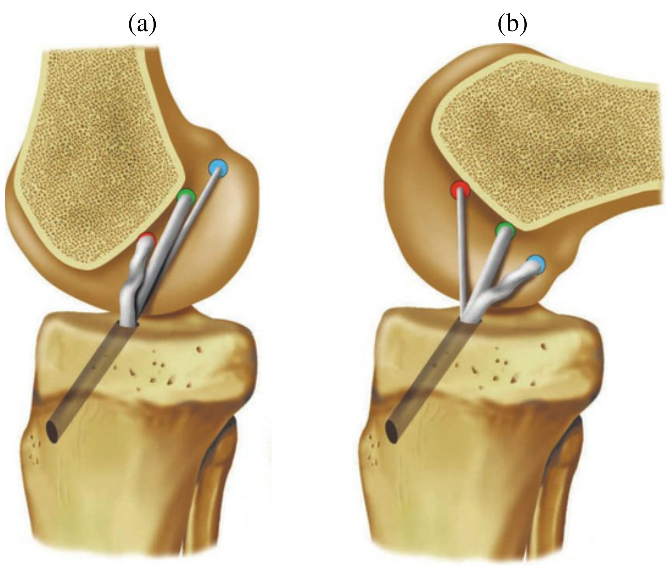

Figure 2.7: Influence of femoral tunnel positioning on graft biomechanics. Identification of anterior (red), isometric (green), and over-the-top (blue) footprints in extension (a). Representation of graft length variations and tension during knee flexion for each positioning strategy (b). Adapted from [36].

Regardless of the drilling method, primary stability depends on the fixation technique. Suspensory fixation utilizes extra-cortical buttons connected to the graft by suture loops, maximizing the amount of tissue within the tunnel (Figure 2.8a). However, it carries risks of tunnel widening due to the transverse oscillation phenomenon known as the "windshield-wiper effect" [7, 34]. On the other hand, compression fixation employs interference screws, made of metal, PEEK, or bioabsorbable materials that force the graft into frictional contact with the bone wall (Figure 2.8b) [7, 37]. In contexts of low bone density, such as in the tibia, hybrid fixation, the combination of suspensory and interference screw methods, is often considered biomechanically superior [7]

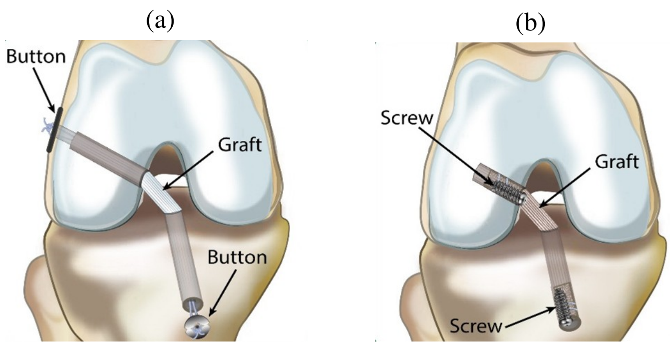

Figure 2.8: Primary fixation methods in ACL reconstruction: Cortical suspensory fixation using buttons on both femoral and tibial sides (a); Compression fixation using interference screws (b). Adapted from [38].

2.3 Current Graft Solutions

As previously noted, graft selection remains one of the most critical decisions in ACLR, directly influencing the joint's biomechanical properties, clinical outcomes, and long-term complication rates [12, 39]. Hence, it is becoming increasingly important to improve the knowledge about each graft for informed and accurate medical decision-making. Broadly, graft options are categorized into three main groups: synthetic grafts; allografts; and autografts.

Synthetic grafts were introduced to eliminate donor-site morbidity and speed up the return to sports. However, non-degradable materials have historically exhibited high failure rates due to stress shielding, fatigue failure, and fragmentation, which can induce reactive synovitis [23, 29]. Recent developments focus on biodegradable devices, known as scaffolds, designed to guide tissue regeneration. However, they still face challenges in balancing degradation rates with restoring the mechanical strength of native tissue [23]. Currently, they are the least commonly used solution.

Allografts, which are harvested from cadaveric donors, have the advantage of reducing surgical time and decreasing postoperative pain because they do not require harvesting tissue from the patient. Despite these advantages, their use is often discouraged in young, active patients due to significantly higher rupture rates, up to three times higher than autografts, the potential risk of disease transmission, and slower biological incorporation and ligamentization processes [15, 39, 40].

Consequently, autografts are currently presented in the literature as the most viable option for primary ACLR [5, 30, 39]. This preference is justified by lower theoretical re-rupture rates and superior biological integration [10, 30]. The three most prevalent autograft options in modern clinical practice, illustrated on Figure 2.9, are the BPTB, HT and, with growing popularity, QT. Each option has distinct morphological and biomechanical characteristics [39, 41]. Beyond structural disparities, these tissues manifest disparate viscoelastic behaviors, meaning that their biomechanical responses to cyclic loads, which are characteristic of human locomotion and quotidian activities, differ considerably among them [12, 23].

The choice among different autograft options is increasingly individualized, considering the patient's activity level, age, and clinical history [39].

The BPTB graft, historically considered the "gold standard" of ACL reconstruction, is made from

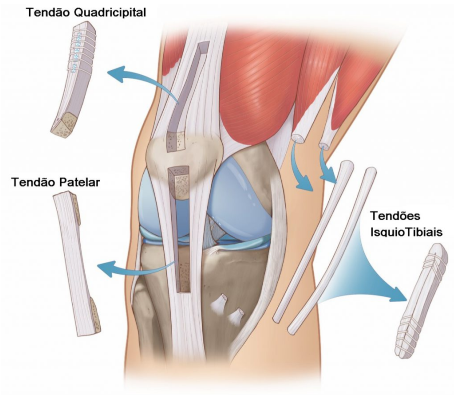

Figure 2.9: Most common autografts in ACLR [42]

the central third of the patellar tendon, which is harvested with bone blocks from the patellar and tibial ends [15, 43]. This configuration facilitates osteointegration through a bone-to-bone interface, allowing for faster and more robust biological incorporation, which is typically completed in approximately eight weeks [41, 44]. Biomechanically, as will be discussed later, the BPTB offers optimal properties. It features structural stiffness that is superior to that of the native ACL. This is fundamental for athletes who require intensive rehabilitation and a rapid return to pre-injury competition levels [12, 23, 39, 45]. Meta-analysis studies involving over 47,000 patients indicate that BPTB grafts have a slightly lower failure rate than hamstring grafts [4]. However, its main disadvantage is donor-site morbidity, which is associated with anterior knee pain, pain when kneeling, and an increased risk of patellar fracture [39, 41, 43]. Additionally, the BPTB graft may be unsuitable for modern surgical approaches, such as the all-inside technique, due to difficulty appropriately shortening the graft length for retro-drilled sockets [33].

Hamstring tendon grafts have evolved from a single strand of one of them to a quadruple-bundle configuration. This configuration uses two bundles of each one. It is currently one of the most popular options. This is due to low donor-site morbidity, smaller incisions, and the absence of anterior pain [39, 41]. It is the preferred autograft for pediatric and skeletally immature populations, although failure rates are comparable to other options in this group [8, 9]. This preference may be more of an attempt to minimize surgical trauma at the harvest site rather than a search for superior biomechanical properties. A critical limitation is the unpredictability of the harvested tendon's diameter. Diameters smaller than 8 mm are associated with a significantly higher risk of failure [46, 47]. Regarding this issue, Dietvorst et al. [48] identified patient height as a significant predictor of tendon length and diameter, serving as an important preoperative planning tool. The disadvantages of the HT include slower bone integration at the tendon-to-bone interface, which takes around 12 to 16 weeks [44]. Other disadvantages include a higher propensity for tunnel widening, persistent hamstring weakness, and a slightly higher risk of postoperative infection due to bacterial colonization compared to the BPTB [39, 45, 49].

Finally, the quadriceps tendon is gaining popularity as a robust and versatile alternative [39, 50]. Morphologically, it is a significantly thicker tendon with a cross-sectional area nearly twice that of its competitors [33, 51]. In procedures such as the all-inside technique, the QT is often preferred due to its large harvestable area and accessibility [33]. Biomechanically, this graft has the highest ultimate failure load [12, 51]. Its versatility allows for harvesting with or without a bone block. It offers clinical results and graft survival rates comparable to other autografts but with substantially lower donor-site morbidity than that observed with the patellar tendon [9, 11]. Despite these advantages, the QT graft presents specific drawbacks that must be considered. Firstly, its harvest is technically more demanding, requiring a steeper learning curve and greater precision to achieve the desired graft thickness and quality [39, 51]. Clinically, while it avoids the severe anterior pain typical of BPTB, it can lead to a temporary deficit in knee extension strength (quadriceps inhibition) during the early stages of rehabilitation, potentially delaying the recovery of thigh muscle atrophy [9, 11]. When harvested with a bone block, there remains a risk of patellar stress fracture, although this is statistically less frequent than in BPTB [39]. Furthermore, some studies report a slightly higher incidence of postoperative hematomas at the donor site due to the vascularity of the suprapatellar region [9]. Finally, although recognized as a high-performance option, the QT still lacks the extensive long-term follow-up data (spanning 15-20 years) that established the BPTB and HT as the historical standards [51, 52].

Table 2.1 synthesizes the overall advantages and disadvantages of the three autologous graft option presented.

Table 2.1: Comparative global overview of BPTB, HT, and QT grafts in ACL reconstruction: clinical status, benefits, and limitations.

Parameter	**BPTB**	**HT**	**QT**
Clinical Status	Historical gold standard	Preferred in pediatric	Increasingly popular
Advantages	• facilitates osteointegration • superior stiffness and strength vs. native ACL • predictable graft diameter • extensive long-term follow-up data	• low donor-site morbidity • smaller incisions • no anterior knee pain • extensive long-term follow-up data	• low donor-site morbidity • highest ultimate failure load • large harvestable area • versatile harvest (with or without bone block)
Disadvantages	• significant donor-site morbidity • increased risk of patellar fracture • poor compatibility with all-inside technique	• slower bone integration • unpredictable graft diameter • greater tunnel widening tendency • persistent hamstring weakness	• higher postoperative hematoma incidence • deficit in knee extension strength • steeper surgical learning curve • lacks long-term follow-up data

2.3.1 Autografts Morphological and Biomechanical Characterization

The success of ACLR is fundamentally dependent on the graft's ability to replicate the complex biomechanical behavior of the native ligament. While tendons primarily attach muscle to bone to transmit contractile forces, and ligaments connect bone to bone to constrain joint motion, both are passive collagenous tissues that function as biological springs under tension. Consequently, they share similar structural characteristics: their fascicles are aligned parallel to the tissue's longitudinal axis and the direction of principal force, conferring highly anisotropic properties. The sinusoidal, wave-like architecture of these collagen fascicles, known as the "crimp" structure, explains their typical non-linear mechanical behavior [23]. This structural similarity is the primary reason why tendons are utilized as grafts in ACLR. Furthermore, due to their high water content, the mechanical behavior of these tissues is generally assumed to be incompressible in computational modeling [53].

While the cruciate ligaments are often simplified as linear cords with point-like insertions for general functional descriptions, such approximations fail to capture their sophisticated biomechanical reactions. The thickness and volume of the ligament are directly proportional to its strength and inversely proportional to its elongation potential; thus, each fiber can be considered an elementary spring [54]. As the morphological and structural properties of the native ACL were discussed in Chapter 2.1, its biomechanical characteristics are summarized in Table 2.2 based on the most widely accepted literature values.

Within the scope of this research, stiffness is defined as the capacity of the graft or native ligament to resist elastic deformation under axial loading. It is quantitatively expressed as the ratio of the applied force to the resulting displacement (N/mm). Stiffness is addressed not merely as a material constant but as a structural property. This characteristic is intrinsically dependent on both the macroscopic geometry of the construct and the microscopic hierarchical organization of the collagen fibers [54].

Table 2.2: Biomechanical characteristics of the native ACL.

Parameter	**Value**	**Reference**
Stiffness	240 N/mm	[12, 23, 29, 39, 55]
Ultimate Tensile Load	2160 N	[29, 34, 39, 55]
Young's Modulus	320 MPa	[35]
Strain at Failure	19% to 36%	[23]

Bone-Patellar Tendon-Bone graft

In contrast to the native ACL, the biomechanical properties of autograft options lack a clear consensus in the literature. For the BPTB graft, reported stiffness values range significantly from 210 N/mm [12] to as high as 1950 N/mm [35], although most frequent values vary between 455 N/mm and 685 N/mm [29, 55, 56, 57, 58]. Similarly, ultimate tensile load reports vary from 1582 N [12] to a more commonly cited 2977 N [29, 34, 50, 55]. It is also important to highlight a significant discrepancy in the literature regarding the Young's Modulus of the patellar tendon between in vivo and *in vitro* studies. While laboratory assays (*in vitro*) frequently report values between 0,2 and 1 GPa [12, 59], measurements in a native environment (*in vivo*) reveal a much higher stiffness, reaching 2,2 GPa [60]. This variation is attributed not only to technical limitations regarding mechanical gripping in the lab but also to biological factors such as hydration levels and the integrity of lateral force transmission between collagen molecules. In the context of ACLR, removing the tendon from its physiological environment and subsequently immersing it in saline solutions can induce tissue hydration, resulting in a temporary reduction of the elastic modulus. This phenomenon must be considered when calibrating computational models, as the effective stiffness of the graft at the time of implantation may differ from properties measured in isolated cadaveric specimens [60].

Table 2.3: Biomechanical characteristics of the Patellar Tendon.

Parameter	**Value**	**Reference**
Stiffness	455 to 685 N/mm	[29, 55, 56, 57, 58]
Ultimate Tensile Load	2977 N	[29, 34, 50, 55]
Young's Modulus	228 to 338 MPa (*in vitro*) 2000 MPa (*in vivo*)	[12] [60]
Strain at Failure	11,4%	[23]

It is important to note that BTPT presents greater stiffness than native ACL and significant decrease of properties when harvested.

Morphologically, the fascicles of the patellar tendon are parallel in the sagittal plane but converge in the frontal plane toward their tibial attachment. Surgeons must account for this tapered morphology, as the graft narrows distally and the fibers maintain an oblique orientation in the coronal plane [61]. The width of this graft is described as significantly decreasing from the proximal to the distal end [50, 62, 63] and Table 2.4 synthesis the most frequently find dimensions of patellar tendon grafts. The thickness of the patellar tendon is non-uniform throughout its length. According to Yoo et al. [63] and studies focused on its insertion sites [31], thickness varies from 3,2 mm proximally to 5,0 mm distally. The tendon is thicker in its central portion (40–75% of its length) and gradually thins toward both edges. Figure 2.10 shows the harvested BPTB autograft, featuring the central third of the patellar tendon and the characteristic bone blocks at the femoral and tibial ends.

Table 2.4: Morphological characteristics of the Patellar Tendon.

Parameter	**Value**	**Reference**
Length	40–60 mm	[62, 63, 64]
CSA	30–35 mm^2	[15, 18, 39, 55, 63]
Thickness	3–5 mm	[31, 62, 63, 64]
Width	24–44 mm	[31, 50, 62, 63]

Figure 2.10: BPTB prepared graft. Adapted from [55]

Hamsting Tendons graft

Several types of hamstring-based grafts are commonly utilized in ACLR. Among them, the quadrupled semitendinosus (ST4) construct exhibits the highest ultimate failure load compared to the quadrupled semitendinosus-gracilis (GST4) or quadrupled gracilis (G4) options. However, an ST4 autograft typically requires a tendon length exceeding 28 cm; in certain demographics, such as female patients, approximately 43,8% of individuals possess ST tendons shorter than this threshold. Furthermore, tripled semitendinosus (ST3) constructs have proven to be biomechanically inferior to four-stranded configurations. Consequently, the most reliable four-stranded construct available is often the GST4 [12]. For these reasons, this section focuses primarily on the GST4, composed of both tendons and their associated muscle components.

Table 2.5: Biomechanical characteristics of GST4 grafts.

Parameter	**Value**	**Reference**
Stiffness	776 to 807 N/mm	[29, 55, 56]
Ultimate Tensile Load	4000 to 4500 N	[12, 29, 34, 41, 55]
Young's Modulus	154 MPa	[12]

Anatomically, the gracilis tendon is approximately cylindrical and is located proximal and superior to the semitendinosus, featuring a rounded muscle belly. In contrast, the semitendinosus is located distal and inferior to the gracilis and possesses a U-shaped muscle belly. During graft preparation, it is recommended that the tendons be twisted in a reverse orientation so that the proximal end of the semitendinosus is adjacent to the distal end of the gracilis, and vice versa [47, 65].

At the microscopic level, hamstring tendons exhibit a homogeneous arrangement of parallel collagen fibers with a planar waveform. Compared to other grafts, they possess a lower fibril density and more widely distributed fibril diameters, with a mean diameter of approximately 125 nm [66]. The distribution and density of collagen fibrils in HT grafts are detailed in Table 2.6.

Table 2.6: Distribution of collagen fibril diameters in Hamstring Tendons [66].

Diameter Interval	**Percentage (%)**
0–50 nm	2,6%
50–100 nm	35,0%
100–150 nm	28,7%
150–200 nm	26,1%
>200 nm	7,6%

Ideally, a graft diameter of at least 8 mm and a minimum length of 7 cm are required for ACL reconstruction; to achieve this, the harvested tendon length should be at least 28 cm [32]. There is a consensus in the literature that the final CSA of an HT graft should range between 53 and 57 mm^2 [12, 15, 18, 50]. Individual cross-sectional area and diameter for gracilis and semitendinosus tendons are presented in Table 2.7.

Table 2.7: CSA and diameter of harvested gracilis and semitendinosus tendons to GST4 grafts [47].

Tendon	**Parameter**	**Value**
Gracilis	CSA	7,15–10,07 mm^2
	Diameter	3,02–3,58 mm
Semitendinosus	CSA	11,33–16,69 mm^2
	Diameter	3,80–4,51 mm

Beyond the advantages previously discussed, HT grafts offer the unique benefit of biological regeneration. The distal tendon of the gracilis muscle has been shown to rebuild after harvesting [34], and the tendons "grow back" in most patients within the first year following a tenotomy [14]. This regeneration occurs in a distal direction, eventually re-establishing attachments to the fascial and tendinous structures of the knee joint. Figure 2.11 illustrates a prepared GST4 graft.

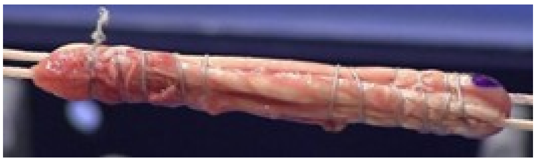

Figure 2.11: GST4 prepared graft. Adapted from [55]

Quadriceps Tendon graft

After being one of the primary choices during the early years of ACL reconstruction, the QT graft has seen a significant resurgence in popularity. While its stiffness is reported as high as 2167 N/mm in some specialized studies [35], the most frequently cited values in the literature fall within a lower range, specifically between 326 N/mm and 463 N/mm [12, 14, 29, 50, 55]. Similarly, values for the ultimate tensile load and Young's Modulus are consistently reported within the ranges of 2186 N to 2353 N [12, 29, 50, 55] and 255 MPa to 370 MPa [35, 67], respectively.

The biomechanical properties of the QT graft are summarized in Table 2.8.

Table 2.8: Biomechanical characteristics of the Quadriceps Tendon.

Parameter	**Value**	**Reference**
Stiffness	326 to 463 N/mm	[12, 14, 29, 50, 55]
Ultimate Tensile Load	2186 to 2353 N	[12, 29, 50, 55]
Young's Modulus	255 to 370 MPa	[35, 67]
Strain at Failure	10,7%	[12]

Histologically, the QT contains 20% more collagen fibrils per cross-sectional area than the patellar tendon. Often considered the "graft of the future," one of its major advantages is its versatility; both the length and cross-sectional area can be tailored to the specific needs of the patient. This is possible because the thickness of the quadriceps tendon is nearly double that of the patellar tendon (PT) in the same individual [51].

The morphological characteristics of the quadriceps tendon are summarized in Table 2.9. Studies utilizing ultrasound to assess the morphometry of the tendon have concluded that it is typically thicker at the proximal end [68]. Furthermore, research by Latiff and Olateju [33] focusing on the harvestable surface area of the QT found that, when measurements are normalized against the length of the patient's limb, metrics for length and width remain highly consistent, with normalized values of 0,096 and 0,060, respectively.

Table 2.9: Morphological characteristics of the Quadriceps Tendon.

Parameter	**Value**	**Reference**
Length	71–89 mm	[33]
CSA	62 mm^2	[55]
Thickness	≈7 mm	[31, 62, 63, 64]
Width	50–57 mm	[33]

Figure 2.12 shows a prepared QT graft.

Figure 2.12: QT prepared graft. Adapted from [55]

In conclusion, the selection of an autograft for ACL reconstruction involves a complex balance between morphological suitability and biomechanical performance. Interestingly, the literature indicates that the primary autografts (BPTB, HT, and QT) are significantly stiffer and stronger than the native tissue they replace. However, for the purpose of computational modeling, it is crucial to recognize that the ultimate strength of the reconstruction is not solely defined by the intrinsic properties of the graft, but by the entire "construct", the graft-fixation-bone complex. Furthermore, the temporal evolution of these properties is a critical factor. Graft strength is at its peak at the moment of reconstruction. However, following implantation, the tissue undergoes a biological process of necrosis and remodeling, known as ligamentization. During this phase, the mechanical properties of the graft temporarily decrease before stabilizing as the tissue adapts to its new functional role [29].

Beyond the intrinsic material properties, a fundamental morphological discrepancy exists between native and reconstructed conditions. While the native ACL exhibits a complex, non-uniform geometry, surgical grafts are typically prepared as cylindrical constructs with a constant cross-sectional area. This geometric simplification in reconstructions may lead to non-physiological strain patterns at the bone-tunnel interfaces and significantly different mechanical behavior compared to the native tissue [69].

Capturing this morphological transition is a key challenge in computational modeling and a critical factor in evaluating the long-term success of the reconstruction.

Understanding these variations is essential for ensuring that the chosen graft can withstand the estimated loads of daily activities, providing a necessary safety margin during the initial stages of incorporation. This characterization serves as the foundation for the finite element analysis, where the interplay between graft geometry, material stiffness, and fixation stability will be evaluated.

2.3.2 Graft Failures

When analyzing overall ACL graft failures, it is possible to try to establish a correlation between their anatomical location and the cause of failure. Proximal ruptures are commonly associated with graft impingement against the intercondylar notch, possibly due to technical errors in tunnel positioning [5, 36]. In contrast, mid-substance tears are predominantly associated with impaired biological ligamentization. Histomorphologically, this biological failure is characterized by structural degradation, including the presence of severe inflammatory reactions and localized tissue necrosis [70]. Lastly, distal failures are considerably less frequent and may be related to mechanical fixation issues or instability at the tibial interface [36].

No such detailed study has yet been conducted on graft failures, but List et al. [71] analyzed 353 cases to assess the frequency of each type of tears of primary ACL rupture. The classification highlighted that midsubstance tears represent the vast majority of native ACL failures, accounting for 52% of cases. Proximal tears and proximal avulsions were also prevalent, representing 27% and 16% of the sample, respectively. In contrast, distal and complex tear types were significantly scarcer, with only 1% and 3%, respectively, of failures being reported. Understanding this distribution in the native ligament is essential, as the high incidence of midsubstance and proximal failures directly influences the biomechanical demands imposed on replacement grafts.

From a biomechanical perspective, computational simulations provide critical insight into these failure patterns. Finite element analyses affirm that a critical deterioration of stress distribution occurs near the articular surfaces, where the graft exits the bone tunnels [69, 72]. This localized stress profile can cause the tunnel wall to mechanically collapse, subsequently enlarging the tunnel [69]. Furthermore, during joint loading, the graft experiences its highest strain values near the femoral distal tunnel port [73]. This matches the regions where maximum stress is distributed on the anteromedial side of the ligament [74]. Ultimately, connecting these mechanical stress maps with clinical data shows how computational models are essential to improve surgical planning and help prevent graft failure.

2.4 Computational Modelling in ACLR (State of the Art)

The use of computational models through the FEM has established itself as a tool of excellence in orthopaedic biomechanics. It allows for the analysis of complex biomechanical scenarios involving diverse bone and ligament geometries, variations in stiffness, and tissue behaviors under dynamic loading conditions. These simulations provide fundamental data that would be extremely difficult, if not impossible, to obtain through direct clinical or laboratory experimentation. Currently, these models provide the necessary scientific support to understand the mechanical factors influencing surgical outcomes, enabling the evaluation and optimization of critical parameters, with the ultimate goal of improving the effectiveness of treatments for ACL injuries [35].

In recent years, computational studies have taken a central role in optimizing the mechanical environment of ACLR. Extensive literature has investigated specific surgical variables, achieving valuable information about both tunnel placement and orientation, that Daniel [16] proved to be decisively indicative of the kinematic and structural response of the joint, and surgical techniques, or even the different options and characteristics of grafts.

Simulations demonstrate that structural behavior is heavily optimized when bone tunnels are aligned closely with the native anatomical footprints [16]. Specifically, finite element literature, including the work of Correia [18], suggests that the ideal tibial tunnel configuration incorporates an inclination of 45º in the sagittal plane relative to the transverse plane, and 30º in the coronal projection relative to the sagittal plane. Furthermore, rounding the entrance edges of the tunnel and applying a slight anteromedial shift (4 mm anterior and 2,5 mm medial from the center) significantly protects the graft structure. In the femoral compartment, positioning the graft footprint posteriorly to the center of the native site has been categorized as a strategic location, resulting in anatomical graft behavior characterized by a low mechanical stress state. According to investigation conducted by Ramos et al. [35], the footprint positioning can influence the maximum load in approximately 20%.

Beyond tunnel location, graft pretensioning and diameter have also been scrutinized. Studies, such as these from Amirouche et al. [75], indicate that anterior tibial translation is best restored to native levels when using a BPTB graft pretensioned with a 60 N force. Regarding graft diameters, the same simulation shows that thicker constructs (> 7 mm) offer high safety margins, whereas thin grafts leave the joint unstable under low loads. The goal to find the best surgical technique and to improve the ones currently used is also covered by FEM studies. Chen et al. [74] and Wang et al. [76] tried to compare techniques such as all-inside, traditional, and transtibial and conclude that none of them could still perfectly restore the original knee. However, the all-inside subjects the graft to less external load and the anatomical reconstruction may better restore anteroposterior stability and contact force with the graft fixed at 0º, while the transtibial technique may better restore knee anteroposterior stability and articular contact force with the graft fixed at 30º of flexion.

However, graft-tunnel interaction remains a primary concern in long-term surgical success. Finite element analysis, for example the one developed by Yao et al. [69], affirms that a critical deterioration of stress distribution occurs near the articular surfaces where the graft exits the bone tunnels, and Zhu et al. [72], demonstrated that during anterior tibial translation, the anterior region of the femoral tunnel aperture undergoes significantly higher pressure compared to the rest of the tract. Both authors, alongside Amirouche et al. [75] agree that this localized stress concentration can cause mechanical collapse of the tunnel wall, leading to subsequent tunnel enlargement over time. Amirouche et al. [75] also showed that while changing the length of the graft inside the tunnel alters the absolute stress and strain distribution on the fixations, showing that a larger volume of graft inside the bone reduces stress on both femoral and tibial anchors, it does not significantly impact overall macro-joint stability under standard tests.

Despite the extensive volume of work analyzing tunnel placement, graft diameters, and fixation mechanics, a critical limitation persists in current computational literature. To simulate joint response, the vast majority of finite element models that compare the native ACL with grafts assume a mechanical equivalence based solely on the global stiffness (K) of the tissue [53]. This assumption introduces a profound geometric paradox. As documented in anatomical studies, the native anterior cruciate ligament presents a highly complex morphology, characterized by a non-constant CSA with a distinct narrowing at its mid-substance and a broad, asymmetrical expansion towards its bone footprints [21, 66] .

In contrast, surgical autografts, whether utilizing the BPTB, HT, or the QT, are mathematically and structurally modeled as idealized, homogeneous cylindrical cords with a constant, uniform cross-sectional area along their entire length [73, 74].

Consequently, there is a gap in understanding how this discrepancy in local geometry alters the internal stress fields and local cinematically driven pressures. An autograft may be engineered to match the precise global structural stiffness of the native ACL. Yet, because its area remains constant while the native ligament's area does not, the local mechanical behavior under flexion, rotation, or anterior translation will be inevitably distinct.

Therefore, establishing a comprehensive biomechanical profile that comparatively maps not only the mechanical properties, such as stiffness, but also the native complex morphology against the uniform geometry of standard clinical grafts is essential.

Chapter 3

Methodology

3.1 Computational Model Development

The computational framework of this study was founded upon a three-dimensional anatomical model of a left knee, specifically comprising the distal femur and proximal tibia, and already validated [35]. To ensure a biofaithful representation of the joint's mechanics, the assembly also integrated the femoral and tibial articular cartilages, alongside the medial and lateral menisci. To optimize visual distinction during the pre-processing and CAD (Computer-Aided Design) modeling phase, a color-coding system was implemented to enhance the segmentation and distinction of the assembly's components: grey for the bones, tibia and femur, pink for the femoral cartilage, yellow for the menisci, and orange for the tibial cartilage. The described 3D assembly and its respective color assignment are illustrated in Figure 3.1.

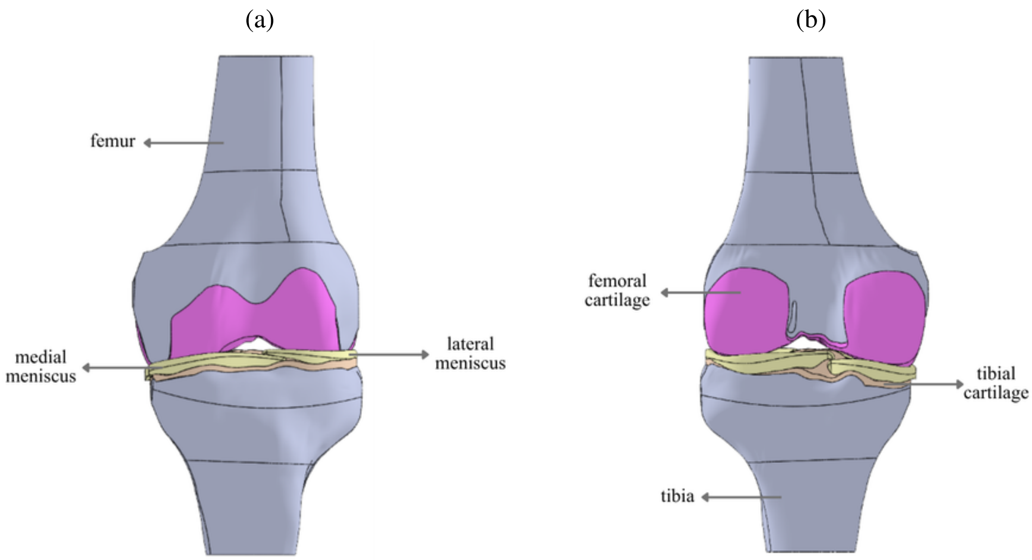

Figure 3.1: Geometric model of the knee joint, serving as the starting point for the simulation. Anterior view (a) and posterior view (b).

It is worth noting that the originally imported anatomical model already featured pre-drilled femoral and tibial tunnels, with their apertures designed to closely mimic the native ligament's anatomical footprints. During the modeling of the native ACL, these geometries served as crucial anatomical references for the placement and orientation of the ligament. However, to preserve structural integrity and prevent interference with the baseline simulation of the intact joint's mechanical outcomes, the tunnels were virtually filled and sealed during this stage.

Furthermore, to decrease computational cost and reduce the overall complexity of the model, the superior portion of the femur and the inferior portion of the tibia were truncated. This geometric reduction effectively decreased the total number of nodes in the model by removing bone regions that would have little to no influence on the stress distribution and mechanical outcomes of the joint areas under analysis. Consequently, the geometry presented in Figure 3.2 represents the final model utilized for the subsequent modulation of the native ACL.

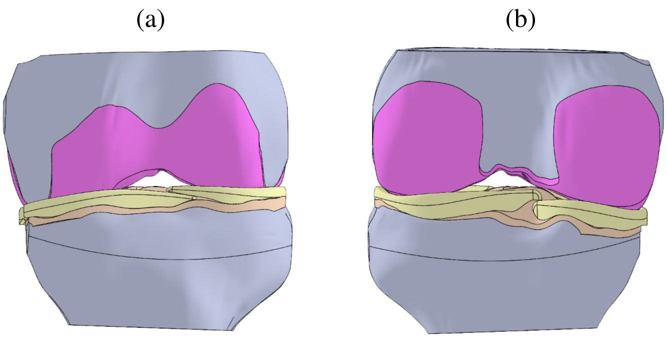

Figure 3.2: Baseline model for the simulation study. Anterior view (a) and posterior view (b).

3.2 Native ACL Modelling

The native ACL was modeled as a single-bundle solid body using SolidWorks2025. The modeling strategy aimed to replicate the ligament's complex anatomical shape, characterized by a narrower mid-substance and broader footprints at the insertion sites [13]. The process was initiated by utilizing the femoral and tibial footprints previously marked on the anatomical model.

An elliptical geometry, rather than a circular one, is justified by the physiological cross-section of the native ACL, which exhibits a non-circular, flattened morphology that significantly influences its mechanical response under tension [66]. The dimensions for each elliptical section were calibrated based on the mean CSA values identified in the literature review [22]. Finally, the ligament volume was trimmed at the bony interfaces to ensure a perfectly flush and conforming contact surface with both the femur and tibia. This approach effectively minimized geometric discontinuities and mimetized the volumetric transitions of the natural ligament, providing a robust solid geometry for the subsequent finite element meshing phase [53].

The geometric parameters of the modeled ligament, including the dimensions of the minor and major axes and the respective cross-sectional areas used in the modeling phase, are detailed in Table 3.1. These cross sections, labeled from Section 1 to Section 5, are ordered sequentially along the ligament's longitudinal axis, progressing from the femoral to the tibial attachment. Additionally, to fully characterize the modeled anatomy, the final characteristics of the reconstructed solid geometry are presented. The length was measured as a straight line between the farthest points of the tibial and femoral insertions. The femoral and tibial insertion areas represent the total contact area between the ligament and bones. The final developed model, which incorporates the native ACL geometry for subsequent numerical simulations, is displayed in Figure 3.3.

Table 3.1: Geometrical properties of the ligament model.

	Axis 1 (mm)	**Axis 2 (mm)**	**CSA (mm^2)**
Section 1	6.38	6.34	34[a]
Section 2	6.75	6.22	33[a]
Section 3	6.70	6.65	35[a]
Section 4	9.45	5.12	38[a]
Section 5	12.18	4.39	42[a]
Length		36.3 mm	
Femoral Insertion Area		89.26 mm^2	
Tibial Insertion Area		83.39 mm^2	

[a] Data from [22].

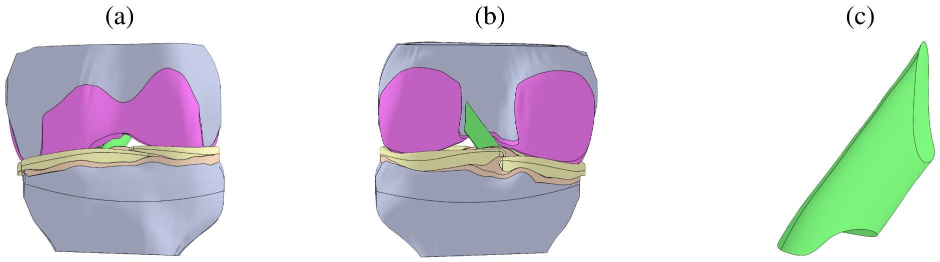

Figure 3.3: Geometric model of the developed native knee joint with ACL: anterior view (a), posterior view (b), and isolated anterior view of the ACL geometry (c).

3.3 Mesh and Material Properties Modelling

Once the geometric model was fully defined, development of the simulation environment could begin. To avoid potential geometric errors and data loss associated with exporting parts and assemblies to external software, the built-in simulation environment within SolidWorks2025 was utilized for this purpose. The followed workflow is presented in Figure 3.4.

Subsequently, the material properties for each knee component were defined, as the software's native library does not include materials with the specific biomechanical characteristics of the joint structures. To reduce computational complexity, initially, a linear elastic constitutive behavior was assumed for all joint constituents. Although biological tissues often exhibit viscoelastic behavior, the adoption of linear elastic properties is a common and validated simplification in orthopedic computational models under low-magnitude loading conditions, such as the ones considered [35, 52, 53]. It is worth noting that while material linearity was prescribed for all materials, treating stiffness as independent of deformation

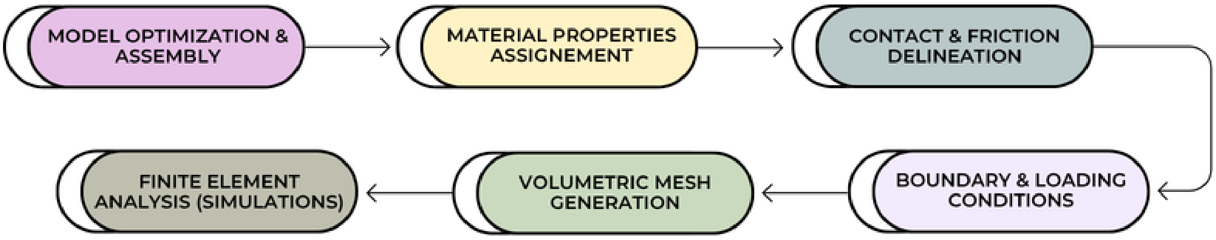

Figure 3.4: Simulation workflow implemented within the SolidWorks2025 environment.

magnitude, the simulations were executed within a nonlinear geometric and contact numerical framework. This means that the solver iteratively updated the structural equilibrium at each load step, accounting for the continuous update of nodal positions under the applied force, while dynamically resolving the evolving contact interfaces between joint surfaces.

The material property values gathered from the literature to define each component are compiled in Table 3.2.

Table 3.2: Mechanical properties of the model materials.

	Cortical Bone	**Trabecular Bone**	**Cartilage**	**Menisci**	**ACL**
Elastic Modulus (MPa)	19650[a]	800[a]	19[b]	59[b]	320[a]
Poisson's Coefficient	0,30[a]	0,26[a]	0,45[b]	0,49[b]	0,49[b]
Mass Density (kg/m^3)	1800[a]	540[a]	1300[b]	1300[b]	1300[b]

[a] Data from [35].
[b] Data from [18].

In addition to material characterization, establishing appropriate boundary conditions through contact interactions between the assembly components is essential for realistic simulations. In this study, a bonded condition was prescribed for most interacting surfaces, ensuring continuous displacement across the interfaces [35, 74].

The exceptions to this approach were the interaction between the femoral cartilage and both menisci, medial and lateral, and the femoral and tibial articular cartilages, as displayed in Figure 3.5. To mimic the highly lubricated, low-friction nature of the physiological joint, these interfaces were defined with a friction coefficient of 0,02, which allows for realistic relative motion between the fibrocartilage and the articular surfaces [35].

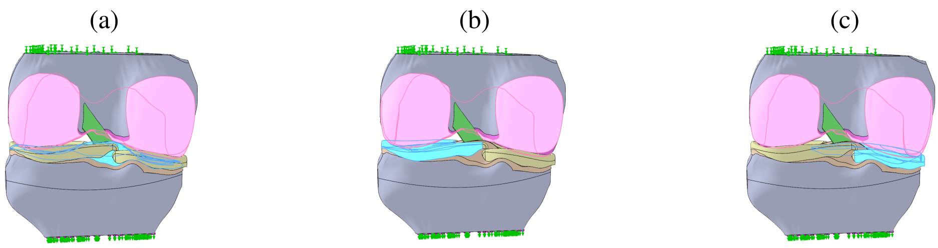

Figure 3.5: Specific low-friction contact interfaces defined in the knee assembly (posterior view): femoral cartilage and tibial cartilage interface (a); femoral cartilage and lateral meniscus interaction (b); and femoral cartilage and medial meniscus interaction (c).

Still regarding the boundary conditions, the superior cross-section of the femur was assigned as a fixed support, as illustrated in Figure 3.6a, to restrict all its degrees of freedom and serve as a rigid anatomical anchor. In contrast, kinematic constraints were imposed on the tibia. Specifically, a roller/slider constraint was applied to the inferior face of the tibia (Figure 3.6b), allowing translational displacement within the transverse plane, and rotation was restricted by constraining the lateral cortical surfaces to remain parallel to the sagittal plane (Figure 3.6c), eliminating the tibia's axial rotation degree of freedom (DoF) . This boundary condition successfully accounts for the secondary stabilizing role of peripheral structures, such as collateral ligaments, omitted from the current joint model. Thus, the introduction of complex torsional stresses was avoided, focusing the study on the primary translational behavior, aligning with standard protocols frequently reported in the literature [53].

(a) (b) (c)

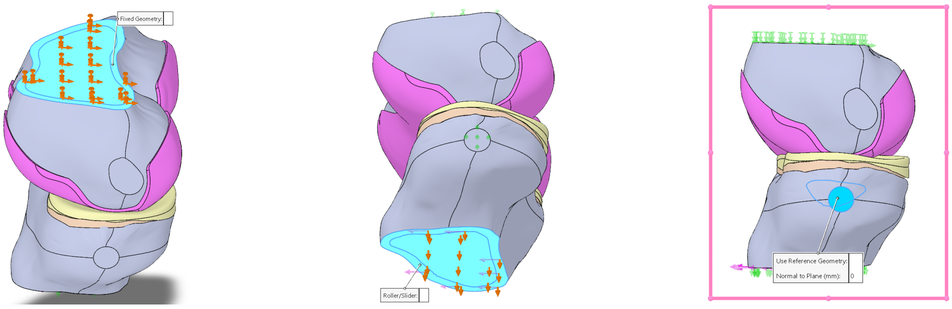

Figure 3.6: Boundary and loading conditions applied. Anterior view showing the fixed boundary condition applied to the femur (a). Lateral view showing the roller/slider constraint applied to the tibial plateau (Roller/Slider-1) (b). Posterior view showing the reference geometry constraint with the sagittal plane (c).

Following the definition of materials and contact interactions, a volumetric finite element mesh was generated for the entire assembly, except for the native ACL.

Due to the complex, organic geometries of the knee joint, tetrahedral elements were utilized to ensure geometric adaptability and prevent artificial stiffening. The discretization process employed a blended curvature-based algorithm, which automatically adjusted the element size to the local topography.

The mesh was constrained by a maximum element size of 13,25 mm in regions of low geometric complexity, while a minimum size of 0,67 mm was enforced to resolve high-curvature features and contact interfaces. To ensure the circularity of anatomical profiles, a minimum of 8 elements per circumference was maintained. Furthermore, a growth ratio of 1,4 was applied to govern the transition between refined and coarse regions, ensuring a smooth gradient that preserves numerical stability. Relatively to the ligament being studied, its mesh was limited to elements until 2,0 mm, to ensure a fine mesh.

Thus, the resulting mesh, showed in Figure 3.7, was characterized by a high density of elements, particularly at the critical interfaces of the articular cartilages, menisci, and the ACL. This ensured that stress distributions and displacement gradients across the joint were captured with the necessary numerical precision for the subsequent analysis. Specifically, the ACL geometry was defined by 707 elements to ensure sufficient resolution for capturing intra-ligamentous strain patterns.

After assembling and discretizing the model, the simulation scenarios were designed to evaluate the ACL's mechanical role during anterior tibial translation. To investigate the effect of variations in the ligament's properties on joint stability, a standardized anterior loading condition was applied. Specifically, a 134 N force was applied to the posterior aspect of the tibia in a posterior-to-anterior direction, as shown in Figure 3.7, similar to anterior drawer maneuver. This load magnitude was selected as it is widely established in biomechanical literature [52, 73, 74, 76] and clinical practice.

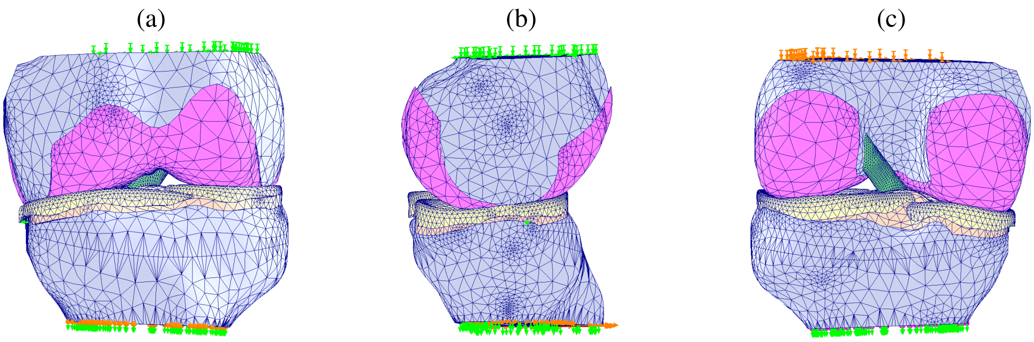

Figure 3.7: Model's resultant mesh and boundary and loading conditions. Anterior view (a), lateral view (b) and posterior view (c).

With the general simulation environment common for all and completely defined, subsequent simulation stages were implemented so that the geometric configuration and the material properties could be studied, with both being systematically altered.

To guide the computational analysis, the simulation workflow was organized into two primary phases. The first phase evaluates the native joint, investigating how the knee responds to changes in the ligament's material stiffness and non-linear behavior. The second phase shifts to reconstruction conditions, examining the impact of replacing the native anatomy with conventional surgical grafts stiffnesses (BPTB, HT, and QT). Beyond the change from a complex shape to a standardized cylinder, this second phase also accounts for the surgical alteration in fixation, modeling a graft anchored inside bone tunnels rather than the native ligament's external insertion.

3.4 The Impact of Stiffness in Native Conditions

To evaluate how structural stability and internal load distribution are impacted by the mechanical properties of the tissue, studies comprising stiffness variations were incorporated into the workflow. According to the Hooke's law for axial deformation and the principles of mechanics of materials, the global stiffness (K) of an axial component is given by:

$$K = \frac{E \cdot A}{l} \tag{3.1}$$

where A represents the CSA, l is the length of the structure, and E is the Young's Modulus of the material [54]. Since the geometric parameters (A and l) of the native ACL model were kept constant during this phase to isolate the influence of material properties, variations in K were achieved systematically by modifying the intrinsic E assigned to the ligament's solid body.

Consequently, three distinct simulation scenarios were performed, each utilizing a different value for the Young's Modulus to understand how the loss or gain of ligament stiffness impacts overall joint biomechanics, particularly regarding anterior tibial translation. The goal was to simulate three distinct contexts broadly representative of physiological or pathological states of the ACL, namely a lax or injured ligament (E = 199 MPa), corresponding to an approximate 37% reduction relative to the normal stiffness value; a normal ligament (E = 320 MPa), representative of an active adult and identified in the literature review (Chapter 2); and a stiffened ligament (E = 465 MPa), corresponding to an approximate 45% increase relative to the normal condition.

The specific Young's Modulus values implemented, along with the corresponding mesh statistics, including the total number of nodes, elements, and DoF for each simulation scenario, are summarized in Table 3.3.

Table 3.3: Young's Modulus and mesh statistics for the different ligament stiffness simulation scenarios.

	E (MPa)	**Nodes**	**Elements**	**DoF**
Lax Ligament	199	184408	108816	548438
Normal Ligament	320	184410	108818	548444
Stiffened Ligament	465	184410	108818	548444

For all three configurations, the non-linear simulation framework was maintained, assuming that the loads were applied gradually and that the constitutive material response remained within the linear elastic range.

An additional scenario was tested in order to understand how a a mechanically negligible ligament acts under the established conditions. For that purpose, a simulation with the same boundary conditions and material properties, except for the ACL's Young's Modulus, was performed. A value of E = 10 MPa was arbitrarily selected as a sufficiently low value to approximate the near-total loss of structural contribution from the ligament.

The joint's mechanical response was primarily evaluated through several key output parameters: displacement; von Mises stress distribution, especially across the ACL volume; equivalent strain along the model; and resultant force in relevant areas of the knee. These metrics were chosen to characterize both the global joint stability and the localized structural demand on the ligament under varying property configurations.

3.5 The Impact of Non-linearity in Native Conditions

Soft biological tissues naturally exhibit hyperelastic and viscoelastic non-linear mechanical behavior, offering low initial resistance under early tensile strains before achieving full structural stiffness. However, for the loads applied in the simulations presented, it is not expected that the ligament deformation goes above the elastic threshold behavior, around 5% [77], in the majority of them. Consequently, employing a fully non-linear formulation across all joint components throughout the entire study would introduce unnecessary computational costs without yielding significant improvements in accuracy.

To scientifically validate this assumption, a single dedicated non-linear simulation scenario incorporating material non-linearity was implemented. In this stage, the linear isotropic elastic constitutive formulation of the ligament was replaced by a non-linear hyperelastic model based on a stress–strain curve of the typical behavior of ACL defined in the literature. This stress–strain curve was adapted from the work of Fernandes [78] (Figure 3.8).

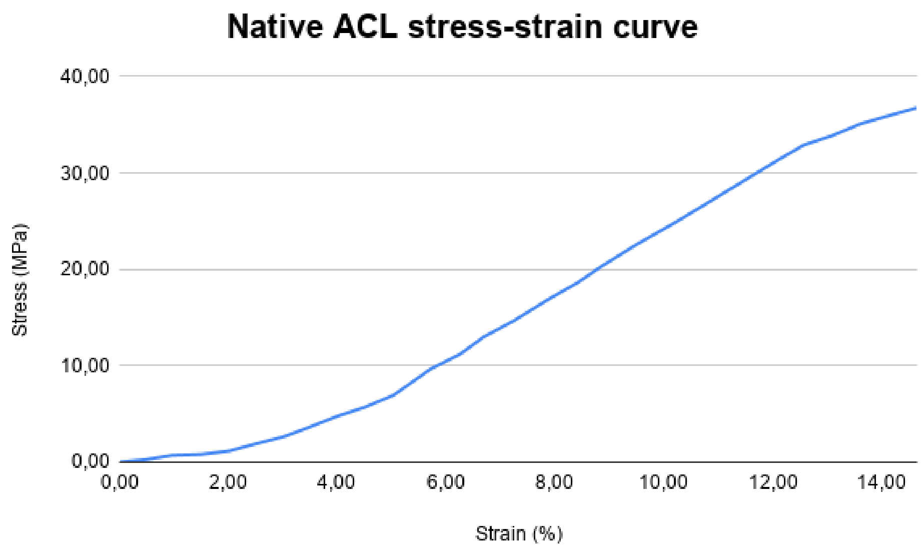

Figure 3.8: Stress-strain curve of the native ACL behavior. Adapted from [78].

Consequently, this setup isolated the hyperelastic material behavior as the sole independent variable to test its impact on joint displacement and stress outcomes.

All other joint structures, boundary conditions, and the 134 N anterior tibial force were kept strictly identical to the baseline setup to isolate the material model as the single independent variable.

The outcomes of this non-linear configuration were cross-analyzed with the linear elastic baseline for the normal ligament scenario.

3.6 The Impact of Stiffness in Reconstruction Conditions

The final phase of the methodological workflow simulated the biomechanical behavior of the various graft alternatives selected in clinical practice for ACLR, presented in Chapter 2.

To replicate the surgical procedure within the computational environment, the femoral and tibial tunnels previously filled, were reopened. These tunnels were characterized by a length of 20 mm and a diameter of 8,4 mm. Furthermore, the tibial tunnel was oriented with a specific inclination of 30º in the coronal plane and 25º in the sagittal plane, and the femoral with 45º in both sagittal and coronal planes, mimicking standard drilling techniques [79].

In contrast with the native ACL, the surgical grafts were geometrically modeled as cylinders with a constant CSA, featuring a diameter of 7,5 mm and a total length of 75 mm. At the exit of the femoral tunnel, a minimum bending radius of 5,2 mm was measured, while at the entry of the tibial tunnel, a radius of 15,0 mm was obtained. The finite element mesh of this isolated graft geometry, with 175020 nodes and 103047 elements, is displayed in Figure 3.9.

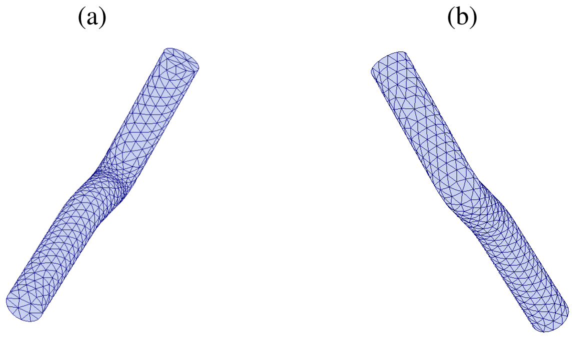

Figure 3.9: Finite element mesh discretization of the isolated cylindrical graft: anterior view (a) and posterior view (b)

To mimetize a rigid and stable surgical fixation, bonded contact conditions were defined exclusively at the terminal boundaries of the tunnels, establishing a continuous displacement interface between the top and bottom faces of the graft and the adjacent bone. Conversely, the interface along the main body of the graft within the intra-articular space and tunnel tracts was characterized using contact interactions with a friction coefficient of $\mu = 0,3$, with both femoral and tibial tunnels [73]. Meanwhile, the intra-articular segments maintained a low-friction interaction ($\mu = 0,02$) consistent with the articular cartilage interfaces. All pre-existing contact interactions and boundary conditions governing the behavior of the bones, articular cartilages, and menisci were kept strictly identical to the previous simulation stages to ensure that geometric and structural variations remained the sole independent variables. Furthermore, the mesh generation parameters for the reconstructed model followed the same guidelines as the previous simulations, resulting in the discretized assembly displayed in Figure 3.10.

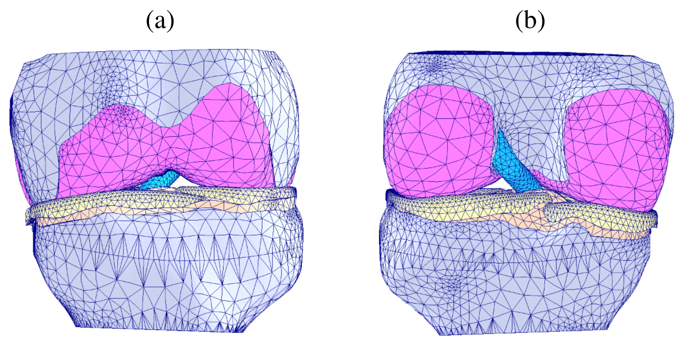

Figure 3.10: Global overview of the final discretized knee assembly model in the post-reconstruction state: anterior view (a) and posterior view (b).

BPTB, HT, and QT were all tested. Their specific E was attributed based on the mid value of the range defined in Chapter 2 for each one and the mass density and Poisson's coefficient were maintained from the native one. Apart from their distinct intrinsic material properties listed in Table 3.4, all other structural characteristics, geometric dimensions, and boundary conditions were kept strictly identical across the three graft simulations to isolate the impact of material stiffness under a constant reconstruction profile.

Table 3.4: Young's Modulus for the different grafts simulation scenarios.

Graft	**E (MPa)**
BPTB	597
HT	154
QT	312

To ensure a direct and consistent comparative assessment, the mechanical response of each graft configuration was evaluated using the exact same output parameters extracted during the native geometry simulations, namely displacement, von Mises stress distribution, equivalent strain, and resultant forces.

In conclusion, this finite element framework ensures a highly controlled environment where meshes, boundary conditions, and anatomical references remain constant, guaranteeing that any variations in joint laxity or intra-ligamentous stress can be directly attributed to changes in tissue stiffness, material non-linearity, or graft geometry. While this systematic isolation of variables establishes a solid foundation for the comparative biomechanical results presented in the next Chapter, it is important to note that the model simplifies certain anatomical aspects. Specifically, the patella, collateral ligaments, and several secondary soft tissues were omitted. Although these approximations are fully justified for low-load and short-duration tasks, they may limit accuracy when simulating more complex or high-load physiological movements.

All the described methodology was developed using SolidWorks2025 software, from the geometric modelling to the definition of the simulation environments. The results of these simulation works are presented and discussed along Chapter 4.

Chapter 4

Results and Discussion

4.1 The Impact of Stiffness in Native Conditions

As previously described in Chapter 3, to assess how the mechanical properties of the native ACL influence the global and local biomechanical response of the knee under the applied load, three simulation scenarios were compared: a lax ligament (E=199 MPa), a normal ligament (E=320 MPa), and a stiffened ligament (E=465 MPa). All three configurations were subjected to the same standardized 134 N anterior tibial load, with identical mesh, boundary conditions, and contact definitions, isolating the Young's Modulus of the ligament as the sole independent variable.

The results of these studies are presented and discussed in the following subsections, divided by the metric under analysis.

4.1.1 Anterior Tibial Displacement

The maximum anterior tibial displacements corresponding to each Young Modulus value are presented in Table 4.1.

Table 4.1: Maximum anterior tibial displacement for each ACL stiffness scenario.

	Lax Ligament	**Normal Ligament**	**Stiffened Ligament**
Maximum anterior tibial displacement (mm)	0,40	0,30	0,26

The maximum anterior tibial displacement decreased consistently as the stiffness of the ligament increased. This inverse relationship between ligament stiffness and tibial translation is consistent with the expected mechanical behavior of the joint [52, 53]. A more compliant ligament offers less resistance to the applied anterior force, allowing greater anterior excursion of the tibia, whereas a stiffer ligament more effectively restrains this translation, reproducing the ACL's primary biomechanical role as the main restraint to anterior tibial displacement [14, 16, 18]. Notably, although the increase in Young's Modulus from the normal to the stiffened scenario (+ 145 MPa) is greater than the increase from the lax to the normal one (+ 121 MPa), the relative reduction in displacement follows the opposite trend. The first transition produced a decrease of only approximately 13%, while the second produced a decrease of almost 27%. This suggests a non-linear relationship between ligament stiffness gain and the resulting restriction of anterior tibial translation, at least within the range tested, with diminishing returns observed as stiffness increases further.

It should be noted that the absolute displacement values obtained are significantly lower than those typically reported by other authors [52, 53, 73, 74, 76] for similar anterior loading conditions, who identified the anterior tibial displacement of native ACL to be between 3 and 6 mm. Possible explanations for this discrepancy include the idealized fixed boundary condition applied to the femur, which removes the compliance normally provided by the surrounding soft tissues and muscular structures, the inclusion of structures such as menisci and cartilage often neglected in those mentioned studies, as well as the linear elastic material formulation adopted for all joint constituents, which may overestimate the overall structural stiffness of the assembly [52, 53]. Nevertheless, the consistent inverse trend between stiffness and displacement remains in agreement with the qualitative behavior described in the literature [52, 73, 74], supporting the validity of the comparative analysis carried out across the simulated scenarios.

4.1.2 Stress Distribution

The maximum von Mises stress recorded across the entire model decreased slightly with increasing ligament stiffness, as presented in Table 4.2.

Table 4.2: Maximum von Mises stress within the joint for each ACL stiffness scenario.

	Lax Ligament	**Normal Ligament**	**Stiffened Ligament**
Maximum von Mises stress (MPa)	26,1	25,3	24,9

In all three scenarios, this overall maximum was consistently located in the medial region of the inferior border of the tibia, indicating that this site is more likely governed primarily by the geometry and boundary conditions of the model, namely the roller/slider constraint and the applied tibial load, rather than by the mechanical properties of the ligament itself.

Focusing specifically on the ACL, a more pronounced trend emerges.

Table 4.3: Maximum von Mises stress within the ligament for each ACL stiffness scenario.

	Lax Ligament	**Normal Ligament**	**Stiffened Ligament**
von Mises stress in ACL (MPa)	9,0	10,0	13,2

According to Zhang et al. [80], for the 134 N applied, the average stress expected in the ACL is between the range of 4,7 to 5,0 MPa, with a peak stress between the range of 9,8 to 10,9 MPa, which aligns with the obtained results, thereby validating the constitutive material models and the overall boundary conditions established in this simulation.

Looking at the data in Table 4.3, there is an increase of approximately 47% between the maximum stress values of the lax and the stiffened configurations, demonstrating the significant impact that ligament stiffness can have on internal stress demand. The von Mises stress distribution maps of the ACL, displayed in Figure 4.1, show that this impact extends beyond the absolute maximum values, also affecting how stress is distributed along the ligament structure.

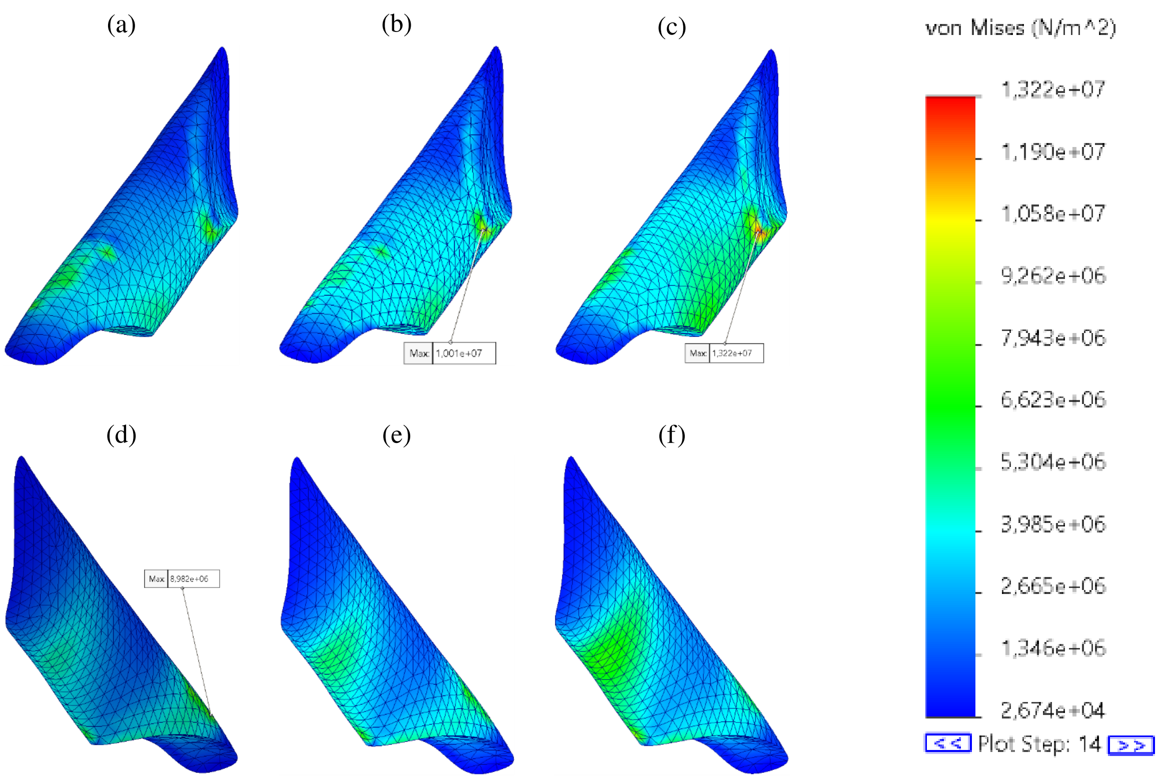

Figure 4.1: Distribution maps of von Mises stress of the native ACL for the lax ((a) and (d)), normal ((b) and (e)), and stiffened ((c) and (f)) configurations. Upper row: anterior face; lower row: posterior face.

On one hand, across all three scenarios, the anterior face of the ligament, near the femoral insertion, consistently exhibits a region of stress concentration, becoming the absolute peak in the normal and stiffened configurations; the posterior face, in the same femoral region, remained uniformly low across the full stiffness range, confirming that this is a markedly localized, one-sided phenomenon [74].

On the other hand, the spatial extent of stress concentration varies considerably with stiffness, particularly away from the femoral insertion itself. In the lax configuration, a second, distinct concentration zone is visible along the distal portion of the ligament, in addition to the femoral peak. This secondary zone corresponds to the precise location where the ACL contacts the infero-posterior region of the femoral cartilage within the intercondylar fossa, the same collision responsible for the global maximum strain discussed below. This secondary region progressively diminishes in the normal scenario and becomes negligible in the stiffened scenario, where the high-stress zone is reduced to a smaller, well-defined area at the femoral insertion. This suggests that, as the ligament becomes stiffer and anterior tibial displacement decreases, the contact between the ligament and the femoral cartilage becomes less pronounced, and the internal load is increasingly channeled into the femoral insertion alone, rather than being partially redistributed toward this distal contact zone.

The maximum principal stress within the ACL followed a broadly similar trend, with values of 9,8

MPa, 11,5 MPa, and 15,3 MPa for the lax, normal, and stiffened scenarios, respectively. The spatial pattern of the principal stress distribution differs from that observed for von Mises stress. As with the von Mises stress in normal and stiffened cases, the peak was consistently located on the anterior face of the ligament, near the femoral insertion, across all three configurations, as shown in Figure 4.2.

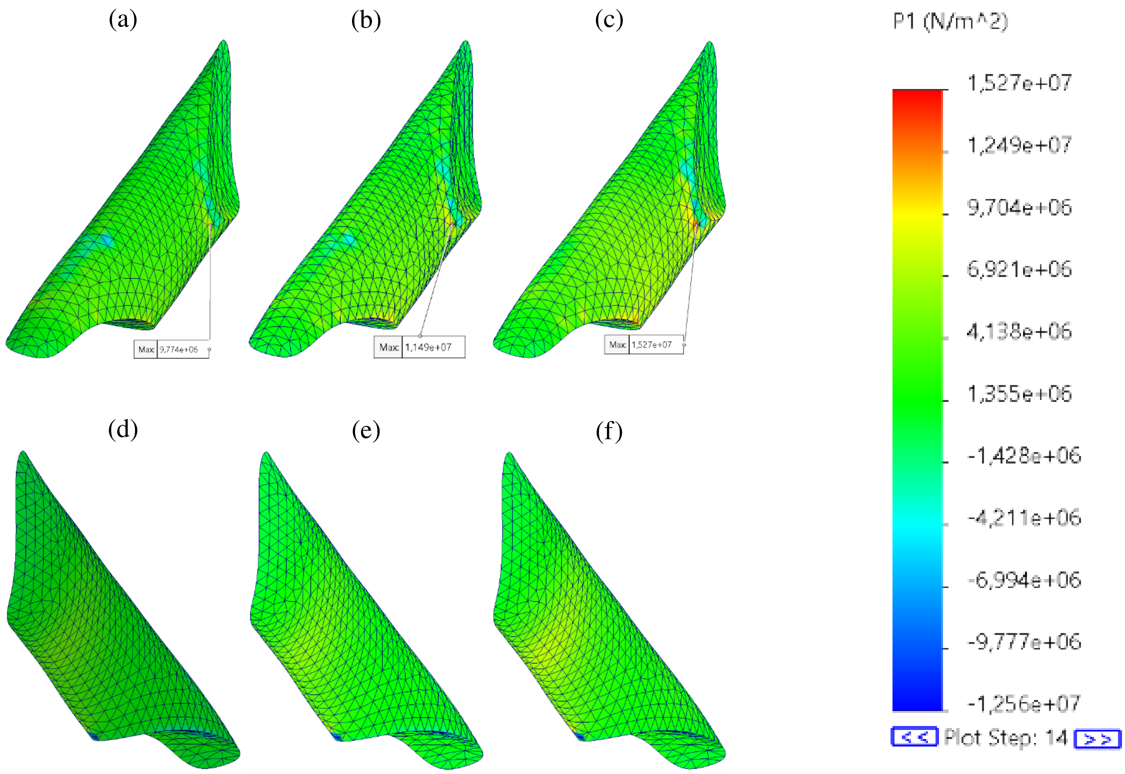

Figure 4.2: Principal stress distribution maps of the native ACL for the lax ((a) and (d)), normal ((b) and (e)), and stiffened ((c) and (f)) configurations. Upper row: anterior face; lower row: posterior face.

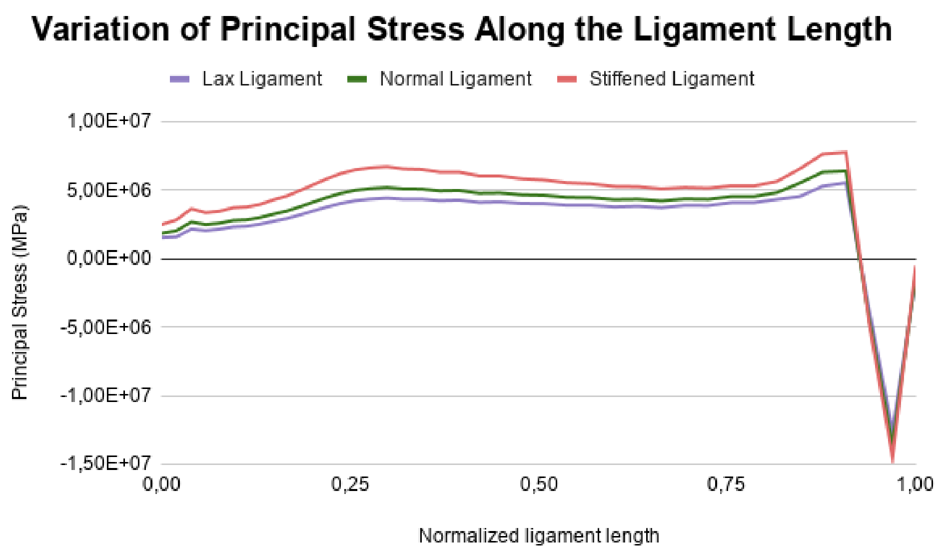

Figure 4.3: Principal stress profile of the shortest edge of the ligament plotted against the normalized ligament length for the lax (purple), normal (green), and stiffened (red) ligament configurations.

In a first look, the principal distribution seems to be identical across all the scenarios. However, focusing on the principal stress distribution along the shortest edge of the ligament, Figure 4.3 shows how the different ligaments accommodated its stress.

Although the three principal stress profiles in Figure 4.3 follow a broadly similar overall trajectory along this edge, rising gradually away from the femoral insertion, remaining comparatively stable across the mid-portion, and inflecting sharply near the tibial insertion, a closer inspection of their local behavior reveals a clear stiffness-dependent pattern. The lax configuration produces the smoothest of the three curves, with comparatively few and modest local oscillations superimposed on this general trend. As stiffness increases, both the normal and, more noticeably, the stiffened configurations display a greater number of pronounced local fluctuations along the same path, indicating that the principal stress is no longer shared evenly among the ligament fibers at this cross-section, but instead alternates more sharply between adjacent zones of higher and lower stress [54]. Since the contour maps in Figure 4.2 no longer convey this spatial distinction once a common stress scale is applied across the three configurations, this oscillatory behavior becomes the most direct quantitative evidence supporting the transition from a comparatively diffuse stress state in the lax ligament toward an increasingly localized one in the stiffened ligament.

Taken together, the von Mises and principal stress maps describe two related but distinct redistribution patterns as ligament stiffness increases. The von Mises distribution evolves from two discrete concentration zones, one at the femoral insertion and one at the distal femoral-cartilage contact site, toward a single, increasingly localized peak. The principal stress distribution, in turn, as captured by the oscillatory pattern in Figure 4.3, evolves from a comparatively diffuse state along the ligament's edge toward an increasingly localized peak at the femoral insertion, without exhibiting a comparable secondary peak at the contact site. This divergence is consistent with the conceptual difference between the two metrics. Von Mises stress is a scalar measure of the combined, multiaxial stress state [54], and is, therefore, highly sensitive to the localized, complex contact stresses generated at the femoral-cartilage collision site. Maximum principal stress isolates the dominant normal (tensile) component along a principal direction, which remains governed primarily by the axial elongation of the ligament fibers near the femoral insertion [54], largely unaffected by this localized contact event. Nonetheless, both metrics converge on the same conclusion: as stiffness increases and anterior tibial displacement decreases, the internal load becomes increasingly confined to the femoral insertion, which emerges as the single dominant site of structural demand [69, 73].

4.1.3 Equivalent Strain Patterns

The global maximum equivalent strain was 24,04%, 18,35%, and 22,21% for the lax, normal, and stiffened model scenarios, respectively. Across all of them, this global peak was caused by the collision of the ligament with the femoral cartilage during anterior tibial translation. Comparing with published literature [52, 76], this contact-driven strain spike is considered to overestimate the physiological response, as the geometric configuration of the tibial insertion in the model resulted in an excessively sagittal orientation of the ligament, exaggerating this collision.

When this localized contact artifact is excluded, no other knee structure besides the ligament itself exhibits strain above 1%, with the exception of the region of the tibial cartilage in contact with the ligament insertion [52, 76]. For this reason, the strain analysis presented in this section focuses specifically on the ACL.

Within the ACL, the maximum equivalent strain was 3,75%, 2,48%, and 2,25% for the lax, normal, and stiffened configurations, respectively, following the same inverse relationship with stiffness observed for displacement.

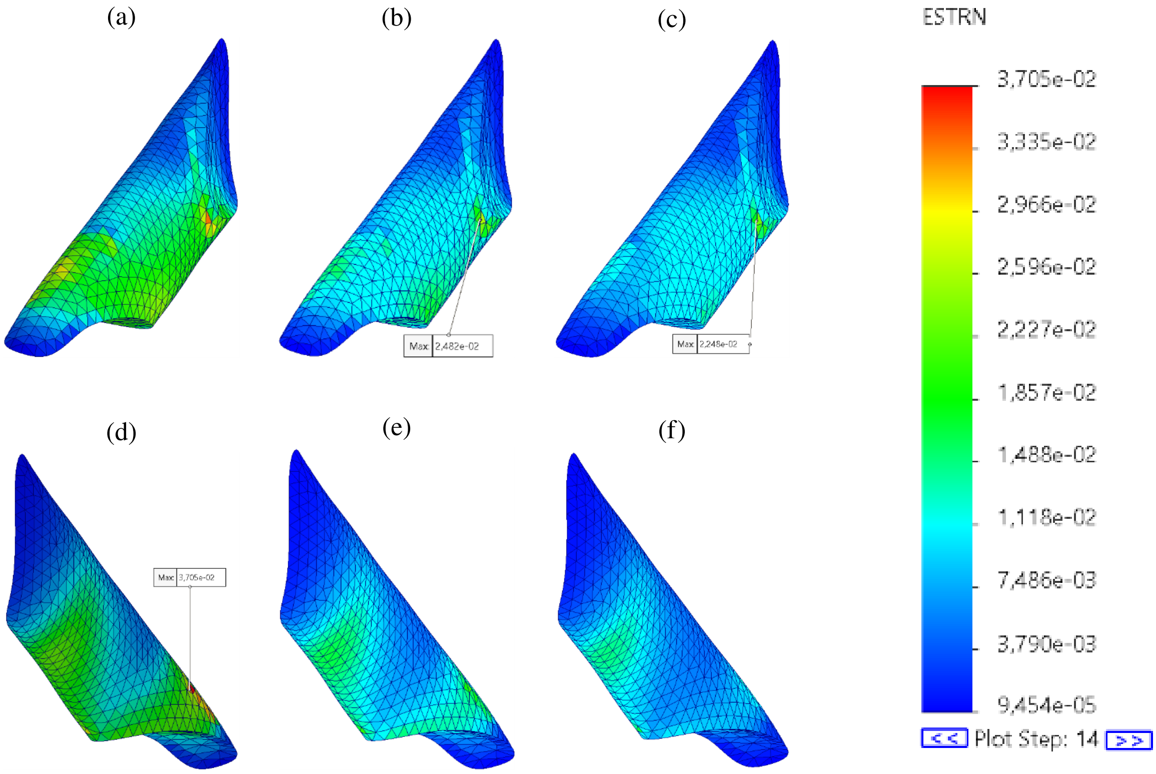

Figure 4.4: Equivalent strain distribution maps of the native ACL for the lax ((a) and (d)), normal ((b) and (e)), and stiffened ((c) and (f)) configurations. Upper row: anterior face; lower row: posterior face.

The strain distribution maps, shown in Figure 4.4, reveal a notable shift in both the location and the face of the ligament where the maximum occurs, mirroring the peak location zones identified in the von Mises maps.

As with the von Mises stress, the location of this maximum shifted from the femoral cartilage contact point, for the lax scenario, to the femoral insertion, in both normal and stiffened scenarios. This shift is consistent with the displacement results discussed in Subsection 4.1.3. In the lax configuration, the greater anterior tibial translation results in a more pronounced collision between the ligament and the femoral cartilage at this distal contact point, and the strain generated there exceeds even that of the femoral insertion, becoming the global peak. As the ligament stiffens and overall displacement decreases, this femoral cartilage collision becomes less pronounced, the contact-driven strain peak diminishes, and the femoral insertion re-emerges as the dominant site of structural demand, aligning with the stress concentration site identified previously. This further reinforces the femoral insertion as the principal site of structural demand under normal physiological stiffness conditions, while highlighting that under excessively compliant conditions, the contact-driven kinematics of the joint can temporarily override this pattern [52, 53].

Beyond the peak values, the strain maps also show that the high-strain region narrows considerably with increasing stiffness, mirroring the trend observed for the von Mises stress: the lax configuration exhibits a broader area of moderate-to-high strain spanning both the distal contact zone and the femoral insertion, which progressively contracts into a single, sharply localized region at the femoral insertion in the stiffened scenario.

Overall, the stress and strain analyses converge on a consistent picture of the native ACL's mechanical behavior across the tested stiffness range. The femoral insertion emerges as the principal site of structural demand [52, 69, 73, 74], regardless of the metric considered, which is consistent with this region corresponding to the narrowest cross-sectional area of the modeled ligament geometry (Section 1, Table 3.1). This suggests that the reduced CSA at the femoral footprint contributes to its identification as the critical region, independently of the contact-driven effects discussed above. Under lax conditions, however, the increased anterior tibial displacement introduces a secondary mechanical demand at the distal femoral-cartilage contact site, which can locally exceed the demand at the femoral insertion itself, depending on the metric considered. As stiffness increases, this contact-driven contribution diminishes, the overall distributed demand does too, and the femoral insertion consolidates as the single dominant site across all three metrics. This combined geometric and contact-driven explanation reinforces the femoral insertion as the critical region for native ACL integrity under anterior loading, while highlighting that, for compliant ligaments, additional distributed demand should not be overlooked [69, 73].

4.1.4 Resultant Forces at Bone Insertions

Table 4.4 presents the resultant forces at both the femoral and the tibial insertions for each simulated scenario.

Table 4.4: Resultant forces in femoral insertion and tibial insertion for each ACL stiffness scenario.

	Lax Ligament	**Normal Ligament**	**Stiffened Ligament**
Resultant Force at Femoral Insertion (N)	84	71	110
Resultant Force at Tibial Insertion (N)	130	124	144

Among all three scenarios, the force transmitted at the tibial insertion was consistently higher than that at the femoral insertion. This is in agreement with the stress and strain findings above, identifying the femoral region, rather than the tibial one, as the site of peak internal stress and strain concentration: a larger share of the load appears to be transmitted through the tibial footprint, while the femoral footprint experiences comparatively lower resultant force but higher localized stress [54].

Unlike the displacement, stress, and strain results, the insertion forces did not vary monotonically with stiffness [52]. Both the femoral and tibial forces decreased from the lax to the normal scenario, before increasing markedly from the normal to the stiffened scenario. This non-monotonic behavior contrasts with the otherwise consistent inverse relationship between stiffness and the other evaluated parameters.

This interpretation suggests that the normal stiffness value, corresponding to the reported properties of the native ACL in the literature, may represent an optimal balance between ligament deformation and load transfer at the ligament insertion, whereas both the lax and stiffened configurations shift this balance toward higher reactive forces at the bone-ligament interfaces, albeit through different mechanisms. This hypothesis, however, would benefit from additional simulation points across the stiffness range to confirm whether this non-monotonic pattern is genuinely a localized minimum around the normal condition, or an artifact specific to the three discrete values tested.

4.2 The Impact of a Non-functional Ligament

An additional simulation was performed using a low Young's Modulus (E = 10 MPa) for the ACL. This arbitrary value intended to approximate a near-total loss of its structural contribution and, thereby, assess how the joint behaves once the ligament is effectively ceases to functions as a load restraint.

Unlike the three native simulations discussed before, this one did not reach numerical convergence for the full 134 N anterior tibial load. The solver could converge only up to approximately 80% of the prescribed force, reaching almost 108 N, beyond which equilibrium could no longer be achieved. All results in this section correspond to this partial loading stat and should not be directly compared, in absolute terms, with the full load results presented for the lax, normal and stiffened ligaments.

Table 4.5 presents the results obtained for this simulation.

Table 4.5: von Mises and principal stress and strain maximums of the non-functional ligament scenario under approximately 108 N.

Max. von Mises stress in ACL (MPa)	Max. principal stress in ACL (MPa)	Max. equivalent strain in ACL (%)	Resultant force at femoral insertion (N)	Resultant force at tibial insertion (N)
20,1	21,0	137,8%	21	63,3

Firstly, the maximum equivalent strain recorded within the ligament reached 137,80%, a value far beyond the failure strain range reported in Chapter 2 for the native ACL. This is the most plausible explanation for the convergence failure experienced, once the ligament's strain state moves to a range so far from where the strain elastic formulation is valid, the solver was likely no longer able to find an equilibrium configuration for further load increments.

Consequently, the von Mises and principal stress values reported within the ligament (20,1 MPa and 21,0 MPa, respectively) should not be interpreted as physically meaningful predictions of the mechanical state of a tissue with E = 10 MPa. A linear stress–strain relationship applied at such a large strain cannot be predictable of what would physiologically happen. These values are therefore reported here primarily as a record of the simulation's numerical behavior rather than as a credible biomechanical result.

The resultant insertion forces, in contrast, seem to be more directly interpretable. At this partial load, the femoral insertion force was 21 N and the tibial insertion force was 63,3 N. In the native scenario evaluated, at the same applied load, the femoral insertion force was already at 68,6 N and the tibial insertion force at 105 N. This evidences that, for the 108 N load, the non-functional scenario only transmitted 19,4% and 58,6% through the ligament's femoral and tibial insertions, respectively. Otherwise, the normal linear scenario, transmitted 63,5% and 97,2% through them. This further reinforce that once the ligament's stiffness becomes negligible, a substantially smaller fraction of the anterior tibial load is carried through its bony attachments, with the remainder presumably redistributed to the surrounding passive structures. Effectively, in normal native conditions, and under a load of 134 N, the menisci and cartilage revealed to support, summing the stress values of each node, 755 MPa. The non-functional simulated scenario, under only 108 N settle, in the same joint structures, 2,6 GPa.

Overall, this scenario should be interpreted primarily in qualitative terms. It supports the expectation that, once the ACL effectively loses its load-bearing capacity considerably less anterior load is transferred through its insertions, consistent with its established role as the primary restraint against anterior tibial translation [14, 16, 18]. However, the very large strains and corresponding stress values computed within the ligament itself fall well outside the deformation range for which the linear elastic material model can be considered valid, and the resulting inability of the solver to reach the full prescribed load reinforces that this configuration represents a numerical limit case rather than a physiologically representative simulation.

4.3 The Impact of Non-linearity in Native Conditions

As described in Section 3.5, a dedicated simulation was performed in which the linear elastic ACL material model was replaced by a non-linear hyperelastic formulation, defined directly from a stress-strain curve representative of the typical mechanical behavior of the native ACL reported in the literature (Figure 3.8). This curve was obtained experimentally and exhibits the characteristic toe-region response of ligamentous tissue, in which low stiffness at small strains progressively increase as collagen fibers become recruited and aligned [78]. The objective of this scenario was to test whether the linear elastic, small-deformation assumption adopted for the remaining native simulations remained adequate within the strain range expected under the standardized 134 N anterior tibial load, cross-analyzing its outcomes against the linear elastic baseline obtained for the normal ligament condition.

As with the non-functional ligament scenario, this simulation did not converge for the full prescribed load (134 N), reaching equilibrium only up to approximately 80% of the target load ($\approx$ 108 N). Table 4.6 displays the results obtained at this partial load for this scenario.

Table 4.6: von Mises and principal stress and strain maximums of the non-linear ligament scenario under approximately 108 N.

Max. von Mises stress in ACL (MPa)	Max. principal stress in ACL (MPa)	Max. equivalent strain in ACL (%)	Resultant force at femoral insertion (N)	Resultant force at tibial insertion (N)
34,9	36,6	96,4	20,6	63,6

The most outstanding feature of these results is the maximum equivalent strain recorded within the ligament, 96,4%, more than three times higher than the upper bound of the experimentally defined input curve and far beyond the failure strain range reported for the native ACL. This outcome can be understood in light of the fundamental difference between the material formulations in comparison. Whereas the linear elastic model assumes a constant stiffness of 320 MPa, the tangent stiffness of the native ACL stress-strain curve remains considerably below this value across most of the physiological strain range, leading the non-linear model to undergo substantially larger deformations under equivalent loading conditions.

The resultant forces recorded at the femoral and tibial insertions, 20,6 N and 63,6 N, respectively, are close to those obtained for the non-functional ligament scenario. This equivalence suggests that, at the point both simulations reached their load limit, the ligament had effectively stop contributing meaningfully to load transfer in either case.

This parallel behavior indicates that the stress–strain curve employed, does not adequately capture the full mechanical response of the native ligament up to the load levels considered in this study. The outcomes of this scenario are therefore not carried forward into the comparative analysis, and the linear elastic formulation adopted for the remaining native conditions is retained as the primary modelling framework throughout this work.

4.4 The Impact of Stiffness in Reconstruction Conditions

The following results correspond to the three reconstruction simulations, in which the native ACL geometry was replaced by a cylindrical graft anchored within femoral and tibial bone tunnels. Each simulation assigns a distinct stiffness to the graft, representative of the most common and tested autologous grafts, as detailed in Chapter 3 in Table 3.4, while maintaining identical boundary conditions and loading across all cases.

Under the standardized 134 N anterior tibial force, similarity to native conditions and as expected, the tibia underwent an anterior millimetric displacement, stretching the graft and increasing the stress and strain experienced throughout the joint. The results are organized by evaluated parameter and compared across the three graft stiffness configurations. Additionally, outcomes are benchmarked against the normal native ACL simulation to quantify the biomechanical deviation introduced by the geometric and material transition from native ligament to surgical graft.

4.4.1 Anterior Tibial Displacement

The maximum displacement experienced by the tibia in the different scenarios are displayed in Table 4.7.

Table 4.7: Maximum anterior tibial displacement for each graft scenario.

	BPTB	**QT**	**HT**
Maximum anterior tibial displacement (mm)	2,04	2,65	3,76

These numerical values are supported by published literature, such as Peña et al. [52], Benos et al. [53], Wan et al. [73], and Wang et al. [76], that obtained values in the range of 2,3 to 10,48 mm for similar loading conditions. The BPTB and QT results fall within the lower bound of this range, reflecting their higher structural stiffness. Although slightly higher, the HT displacement remains well within the reported range, consistent with its lower Young's Modulus.

Looking at the rest of the joint, the femur remained essentially stationary, consistent with the fixed boundary condition applied to its superior surface. The menisci and tibial cartilage moved in close agreement with the tibia, confirming the kinematic continuity of the joint under anterior loading. For the graft, the displacement profile is coherent with the rest of the structures, it is lower at the femoral site and continuously grows until the tibial site. Selecting the same node of its intra-articular mid-portion across all the simulations, values of 1,86 mm, 2,39 mm and 3,36 mm were extracted from BTBP, QT and HT displacement, respectively.

Once again, the results reveal a clear inverse relationship between graft stiffness and anterior tibial displacement. This trend is consistent with the native stiffness analysis and reinforces that, regardless of geometric configuration, structural stiffness remains a primary determinant of joint translational stability under anterior loading [52, 53].

The difference of stiffness across the three grafts in analysis provides diverse displacement responses to the applied 134 N anterior load. This differences are not exclusively related to the maximum tibial displacement, but also of the dynamic behavior across the increment of the imposed force. In this regard, Figure 4.5 illustrate the anterior tibial translation evolution as a function of simulation time. It was evaluated in the same tibial node across all configurations.

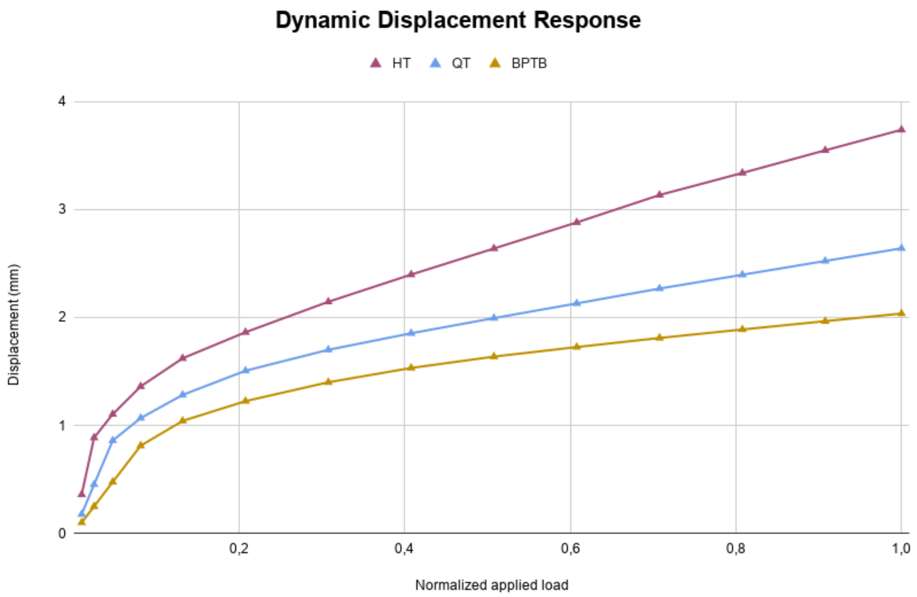

Figure 4.5: Tibial displacement of each graft configurations as a function of the normalized anterior applied load (where 1 corresponds to 134 N).

All three configurations exhibit a nonlinear displacement response as the aplied anterior force increases.

The BPTB graft, owing to its highest Young Modulus, presents the lowest rate of displacement growth across the entire loading range, always with the overall slightest slope. This indicates that the graft engages rapidly and resists deformation effectively even at low force magnitudes, providing consistent translation constraint throughout the loading spectrum. The QT shows an intermediate response, with a steeper initial slope compared to BPTB but converging toward a more moderate rate of increase at higher load fractions. The HT graft, as the most compliant one, reveals the steepest slope throughout the load scale, accumulating displacement faster at each increment than the opponents, and reaching the highest final translation, as presented before.

This behavior reflects the greater initial yielding characteristic of lower-stiffness materials, which require more deformation before developing sufficient resistive force to stabilize the joint [73]. The early divergence of the three graft options behavior further reinforces the clinical relevance of graft stiffness selection, as inadequate stiffness not only affects maximum laxity but can also compromise joint stability across the entire range of physiological loading conditions [12, 39].

4.4.2 Stress Distribution

The von Mises stress distribution maps acquired across the reconstructed knee models are shown in Figure 4.6, with their absolute maximum values explicitly labeled.

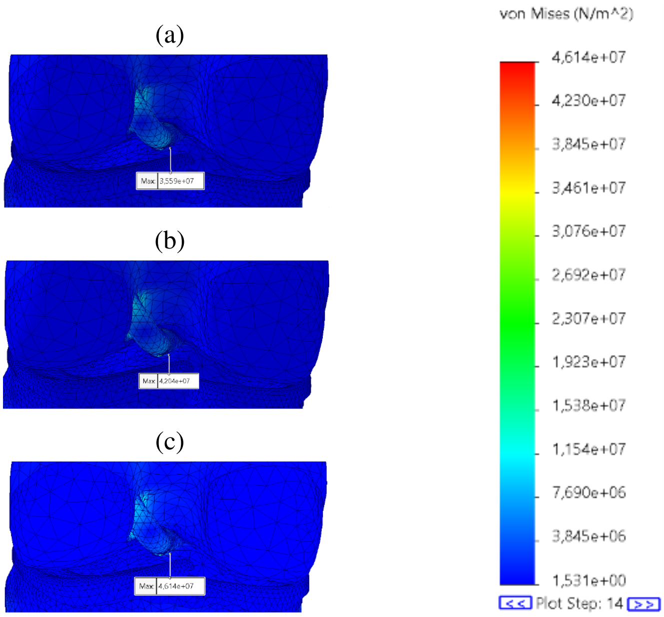

Figure 4.6: Posterior view of von Mises stress distribution maps of the BPTB (a), QT (b), and HT (c) configurations.

Additionally, to closely evaluate the internal structural demand on the surgical replacements, the isolated stress profiles along the grafts bodies are also illustrated (see Figure 4.7).

The peak values extracted from these numerical simulations are compiled and summarized in Table 4.8 for a direct comparative assessment.

Table 4.8: Maximum von Mises stress within the joint and the graft for each graft scenario.

	BPTB	QT	HT
Maximum von Mises stress in the joint (MPa)	35,6	42,0	46,1
Maximum von Mises stress in the graft (MPa)	32,0	27,5	26,8

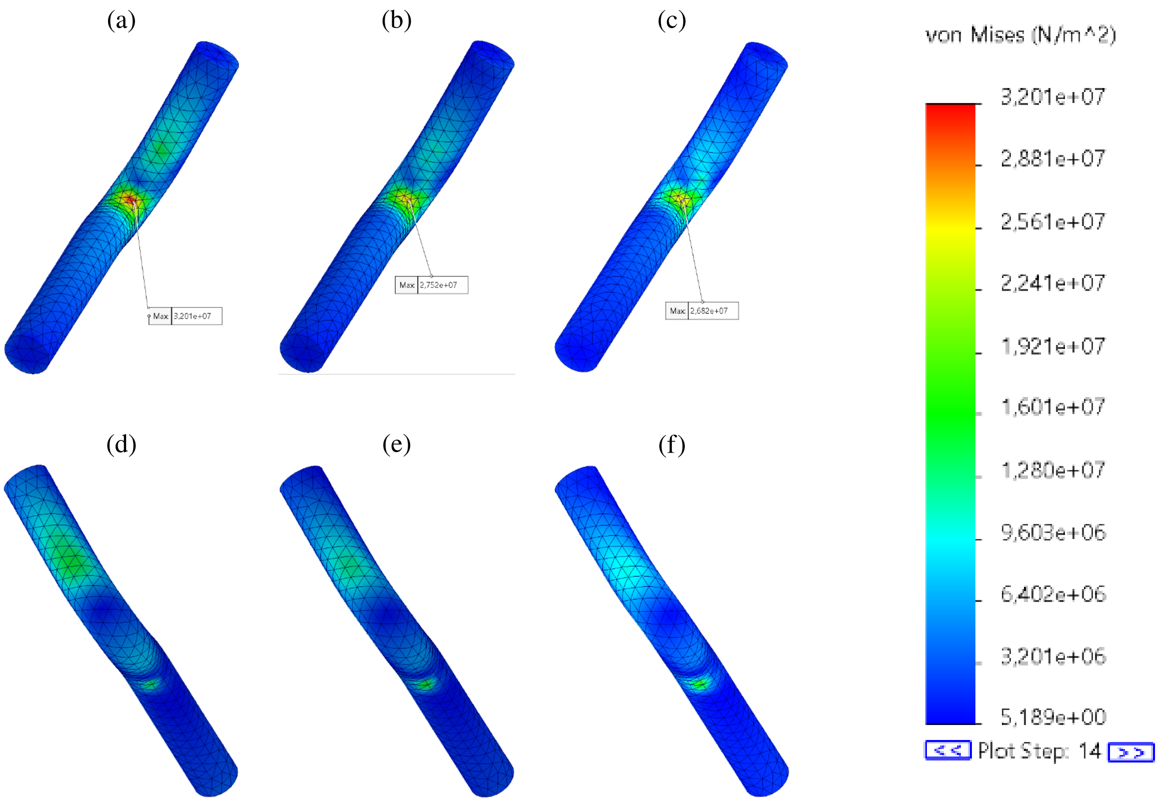

Figure 4.7: von Mises stress distribution maps of the BPTB ((a) and (d)), QT ((b) and (e)), and HT ((c) and (f)) configurations. Upper row: anterior face; lower row: posterior face.

The von Mises stress distribution across all reconstruction simulations consistently identified two distinct concentration zones: the posterior aspect of the tibial tunnel entrance, where the highest stress values in the overall model were recorded, and the anterior aspect of the femoral tunnel exit, where peak intra-graft stress was concentrated. This spatial pattern is partially consistent with findings reported by Yao et al. [69], Zhu et al. [72], and Wan et al. [73], who identify the femoral tunnel aperture as a critical stress concentration site, and further highlights the tibial tunnel interface as an additional region of biomechanical concern under anterior tibial loading. Although the absolute peak stress of the model is located at the tibial tunnel entrance, the area surrounding the anterior exit of the femoral tunnel is more distributively affected, which aligns with those published findings.

Regarding peak stress at the tibial tunnel entrance, values of 46,1 MPa, 42,0 MPa, and 35,6 MPa were recorded for the HT, QT, and BPTB grafts simulations, respectively. This evidences an inverse relationship between graft stiffness and bone-interface stress. Mechanically, this suggests that more pliant grafts (such as the HT) transfer a higher proportion of the applied load to the surrounding bone matrix [53, 73]. This phenomenon increases the localized mechanical demand at the fixation site, which clinically translates into an elevated potential risk of tunnel widening over time [34, 69]. Conversely, the von Mises stress peaks intra-graft at the femoral tunnel exit followed the opposite trend, with the BPTB recording the highest value (32,0 MPa), followed by the QT (27,5 MPa) and the HT (26,8 MPa). This pattern indicates that stiffer grafts absorb a larger share of the anterior tibial load internally, concentrating stress within the graft tissue itself rather than transferring it to the bone interface [52, 73].

This opposing trend, illustrated in Figure 4.8, between intra-graft and interface stress constitutes a fundamental biomechanical trade-off: grafts with higher stiffness protect the bone-tunnel interface at the cost of increased internal stress, while more compliant grafts distribute load to the fixation sites, potentially compromising long-term tunnel integrity [34, 69, 72].

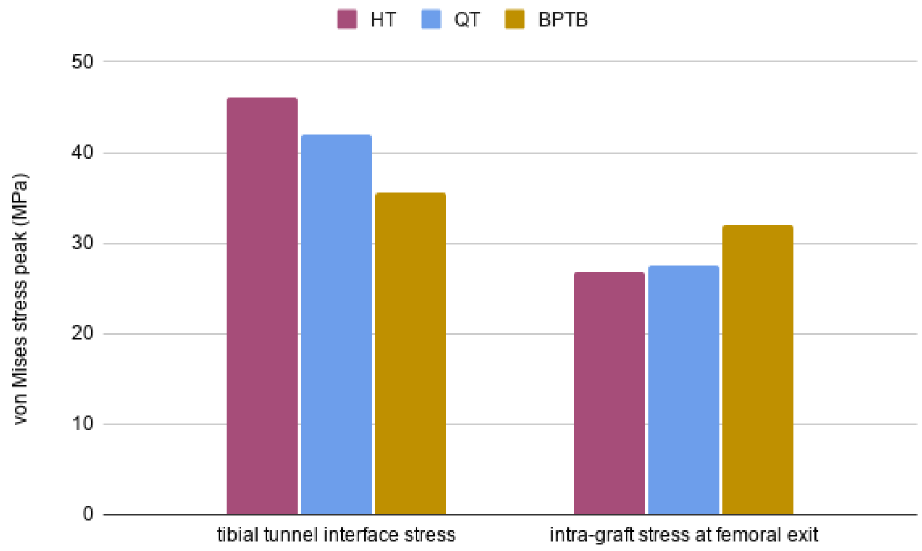

Figure 4.8: Peak von Mises stress at the two primary stress concentration sites for each graft configuration. The tibial tunnel interface stress on the left and the intra-graft stress on the right.

The maximum principal stress results throughout the graft body reinforce this interpretation (Figure 4.9).

Both BPTB and QT exhibit their highest stress concentration, 41,4 MPa and 34,8 MPa, respectively, precisely at the large angulation at the entrance of the femoral tunnel into the intra-articular space. In contrast, for the more compliant HT configuration, the stress peak shifts partially toward the tibial tunnel (35,2 MPa). This behavior suggests a stiffness-dependent redistribution of load between the two fixation sites. Because the HT is more flexible, it initially yields and stretches under the applied load, which slightly delays its full mechanical engagement [12, 73]. This compliance allows for a greater initial anterior translation of the tibia, as seen before in Figure 4.5. As the tibia shifts forward, the graft undergoes a more pronounced angular change, more flexible structures transfer the mechanical burden along its body, rather than retaining the stress at the femoral exit, resulting in the higher peak stress recorded at the tibial tunnel entrance [72, 73, 74].

Analysis of the mid-portion of the grafts revealed a highly uniform and low stress distribution, indicating that the intra-articular segment safely accommodates the structural load [73, 74]. Furthermore, the segment of the graft length located inside the bone tunnels remained largely shielded from high stress states.

Beyond the graft and tunnel interfaces, the articular cartilages and menisci were also examined for evidence of load transfer to the peripheral joint structures (see Figure 4.10). It should be noted that the color scale applied to this figure was deliberately narrowed relative to that used for the graft and tunnel stress maps (Figures 4.7 and 4.6), since the absolute stress magnitudes recorded within the cartilage and

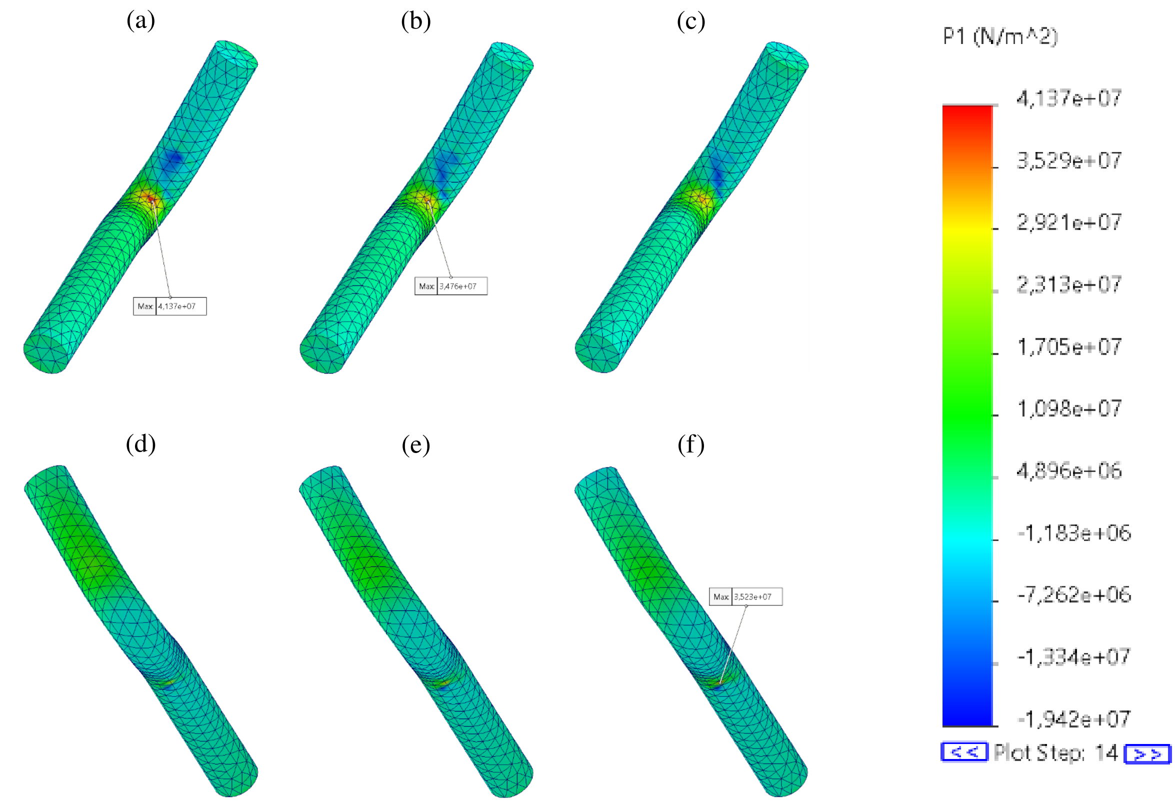

Figure 4.9: Principal stress distribution maps of the BPTB ((a) and (d)), QT ((b) and (e)), and HT ((c) and (f)) configurations. Upper row: anterior face; lower row: posterior face.

menisci are substantially lower that those concentrated at the tunnel apertures and within the graft body (Table 4.8). This rescaling was necessary to expose the comparatively subtle variations occurring within these peripheral tissues, which would otherwise appear uniformly low, and therefore indistinguishable, under a shared scale spanning the full range of joint stresses.

Within this adjusted scale, the peak von Mises stress recorded in the cartilage and menisci was 7,1 MPa, 8,2 MPa, and 11,1 MPa for the BPTB, QT, and HT configurations, respectively, revealing a clear inverse relationship with graft stiffness. Although these values remain considerably below the peaks identified at the tunnel apertures and within the graft itself (35,6 to 46,1 MPa, Table 4.8), their progressive increase with decreasing stiffness indicates that the surrounding articular structures are not entirely insulated from the mechanical consequences of graft selection. This trend is particularly evident in the spatial distribution shown where the elevated stress remains tightly confined to the immediate neighborhood of the tunnel apertures in BPTB (4.10a) scenario, whereas in the HT scenario (4.10c), an additional region of elevated stress becomes visible in the medial compartment, away from the structures directly bordering the graft pathway, an involvement essentially absent in both BPTB and QT maps.

This indicates that, as the graft yields more readily under the applied force, a larger share of the anterior tibial load is absorbed by the surrounding passive structures of the joint. Changing the graft type between those considered, therefore, does not only dictate the localized stress fields experienced by the stabilizing substitute and the bone tunnels where it is anchored, but also modulates, to a measurable extent, the mechanical involvement of the surrounding cartilage and meniscal tissues [72, 73].

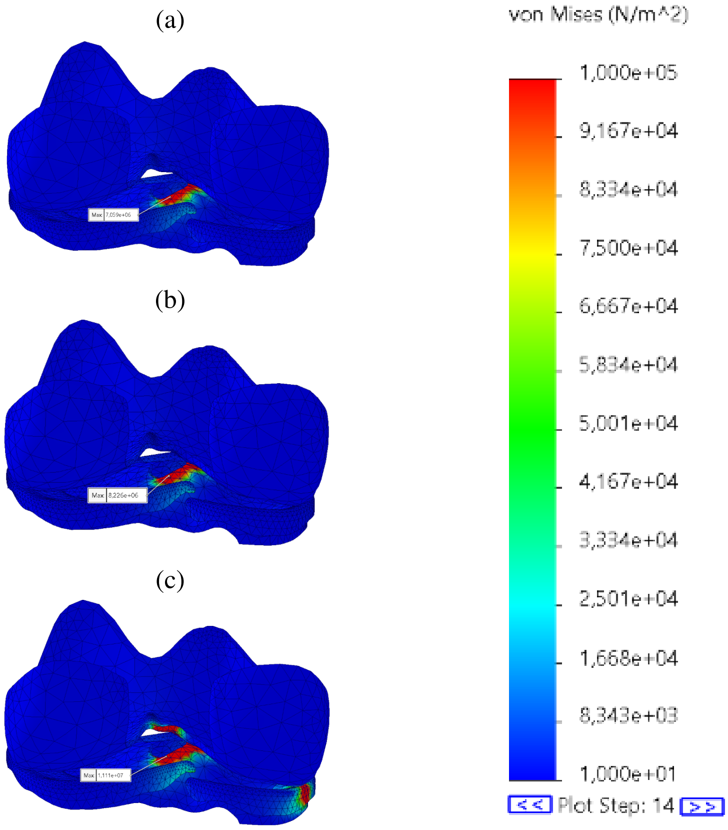

Figure 4.10: Posterior view of von Mises stress distribution maps of the tibial and femoral cartilages and menisci in BPTB (a), QT (b), and HT (c) configurations.

The maximum peak identified in the same metric and area for native conditions was 4 MPa, significantly lower than those identified in reconstruction scenarios, showing that ACLR for itself alters the joint global homeostasis.

4.4.3 Equivalent Strain Patterns

To complement the stress analysis, the structural deformation behavior across the reconstructed models is also evaluated. Similarly with what was done for the native conditions, the equivalent strain was assessed to identify regions vulnerable to excessive elongation or structural yielding under the simulated anterior loading conditions [52, 73].

Regarding the peripheral structures of the knee joint, the strain patterns were found to be negligible. The single exception was a localized strain concentration on the articular cartilage surrounding the tibial tunnel entry. However, this phenomenon was deemed to be not representative of reality, because clinically, during the surgical reconstruction, the surgeon physically debrides and resects any obstructing cartilage at the tunnel aperture before graft insertion to ensure a clear pathway and avoid tissue entrapment [81]. Since this wound care was not geometrically modeled, the excessive localized strain there can be interpreted as a characteristic artifact of the definition of contact interaction. Excluding this specific zone, all remaining bone, cartilage and meniscal tissues of BPTB and QT simulations remained within very low and physiologically safe deformation limits (maximum strain below 0,6%), confirming that joint stability was maintained without damaging the peripheral articular surfaces. For the HT simulation, a value of 4,5% was found in femoral cartilage, probably due to the physical collision with the graft during the simulated displacement.

Therefore, the detailed strain analysis focused exclusively on the three surgical substitutes, as illustrated in the isolated graft maps presented in Figure 4.11, with the respective maximum strain value and location experienced by each.

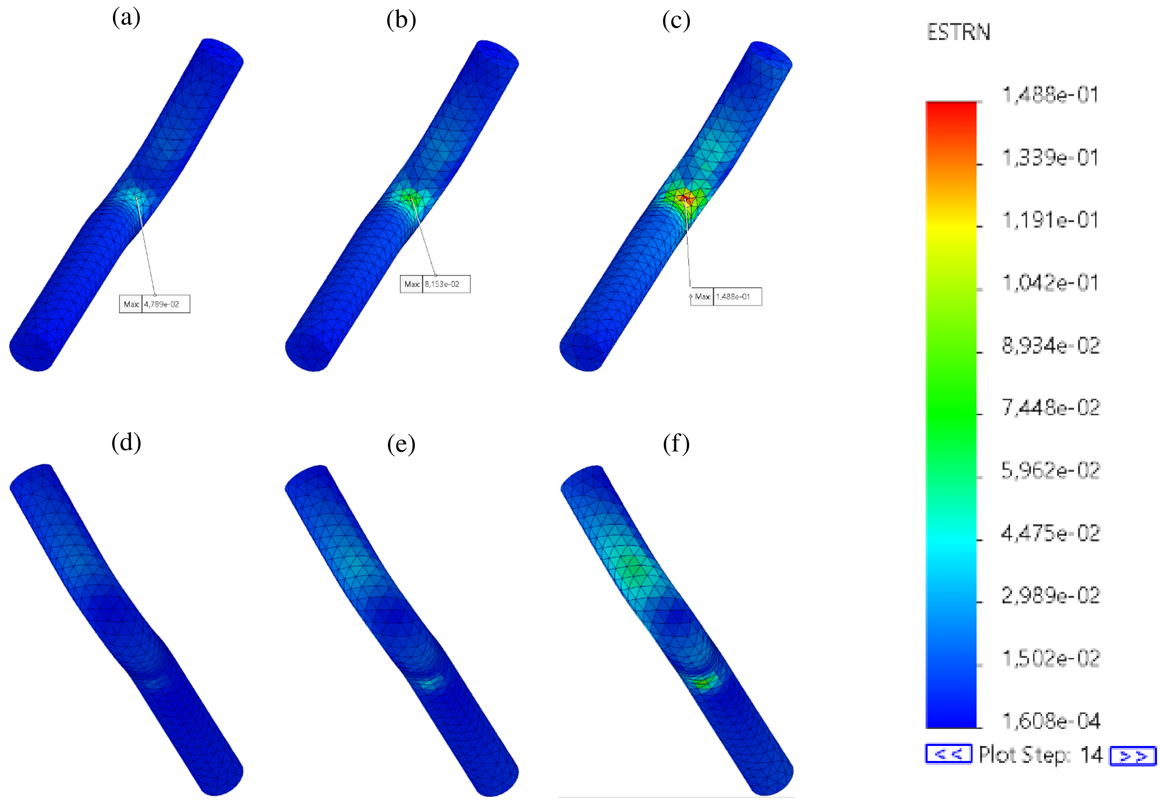

Figure 4.11: Equivalent strain distribution maps of the BPTB ((a) and (d)), QT ((b) and (e)), and HT ((c) and (f)) configurations. Upper row: anterior face; lower row: posterior face.

Across all three graft configurations, the equivalent strain maps reveal a spatially consistent pattern. Strain is overwhelmingly concentrated at the anterior aspect of the femoral tunnel exit, where the graft undergoes its most pronounced angular transition. This localization mirrors the stress concentration identified in the previous subsection and confirms that the femoral tunnel exit is the primary site of structural demand regardless of graft type. Peak equivalent strain values of 4,79%, 8,15%, and 14,88% were recorded for the BPTB, QT, and HT grafts, respectively, at this location, evidencing once again an inverse relationship with stiffness that is consistent with all previously reported mechanical parameters. Thereby, due to its lower stiffness, the HT tissue yields more easily under the applied tension, leading to a marked elongation of its fibers [12, 73]. This increased flexibility forces the main body of the HT graft to stretch and undergo significant deformation to engage the load and stabilize the joint, resulting in the higher joint laxity discussed in previous sections.

This peak values exceed the 5% considered to be, in Chapter 3, the limit of linear elastic behavior of tendinous and ligamentous structures. Thus, simulations considering non-linear behavior could be interesting to develop in future researches.

To further characterize the longitudinal strain distribution, an equivalent strain profile was extracted along a line in the anterior surface of each graft from the femoral to the tibial fixation, as shown in Figure 4.12. The three profiles share a highly consistent morphology. The strain begins to grow gradually within the femoral tunnel tract before rising sharply at the femoral tunnel exit, creating the most prominent peak observed in the graph, which directly corresponds to the red elements illustrated in the 3D contour maps. Past this critical transition, the strain drops rapidly into a low, uniform plateau across the intra-articular mid-portion and continues at a low baseline throughout the tibial tunnel. Notably, the slight strain concentration at the tibial tunnel aperture is not visible in this specific profile because this peak is localized on the posterior aspect of the ligament, where the inner, tight side of the anatomical curvature is located.

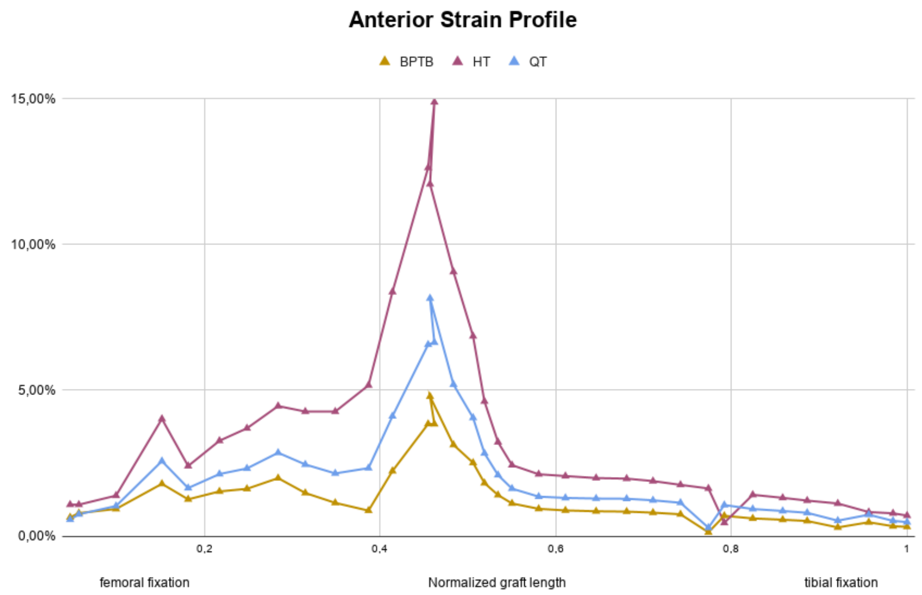

Figure 4.12: Equivalent strain profiles extracted along the anterior surface of each graft, from the femoral to the tibial fixation, as a function of normalized graft length (where 0 and 1 correspond to the femoral and tibial fixations, respectively).

This overall spatial pattern confirms that the structural demand is heavily governed by the geometric transitions at the tunnel apertures rather than solely by the material properties of the graft, since the qualitative morphology remains identical across all three configurations despite their distinct stiffness values. To mathematically quantify these spatial distributions, a numerical integration using the trapezoidal rule was performed to calculate the area under the strain curves, evaluating the proportion of deformation restricted to the critical femoral peak zone relative to the total graft body. The femoral peak area accounted for approximately 37,42%, 40,63% and 42,98% of the total area under the curve for the BPTB, QT, and HT grafts, respectively. These values are remarkably high for all configurations, demonstrating that regardless of the chosen substitute, nearly double the expected proportional deformation is tightly locked within a small geometric window at the femoral exit.

Accordingly, this confirms the expected biomechanical behavior, with the geometric transition acting as the dominant factor governing strain localization, while the specific graft stiffness refines how this deformation is distributed. An higher structural stiffness forces the splitting of mechanical demand more evenly across the graft [52, 69].

4.4.4 Resultant Forces at the Graft-Tunnel Interface

The graft-tunnel interface is one of the most frequently analyzed interactions in ACLR due to its influence on success prediction and long term knee stability [34, 69, 72]. Thus, the resultant forces extracted from the reconstruction simulations are compiled in Table 4.9. It includes the fixation reaction forces at the femoral and tibial tunnel interfaces, and the free body force transmitted through the grafts.

Table 4.9: Resultant forces for each graft scenario.

	BPTB	**QT**	**HT**
Femoral Fixation Force (N)	45,0	44,1	42,6
Tibial Fixation Force (N)	116,3	97,3	73,9
Graft Free Body Force (N)	131,4	114,2	91,7

The tibial fixation force varied substantially across the three graft configurations, progressive decreasing with diminishing graft stiffness. This confirms a direct relationship between construct stiffness and the magnitude of load transmitted to the tibial anchor. This is consistent with the constitutive relationship defined by Hooke's Law, whereby, for a constant imposed displacement, a stiffer construct generates a proportionally higher reactive force at its anchoring interfaces [54]. In contrast, the femoral fixation force remained largely invariant across all three scenarios, presenting a variation of less than 6% for the full stiffness range tested. It is also important to highlight that the tibial fixation force was consistently greater than the femoral one, consistent with what Yao et al. [69] and Zhu et al. [72] reported.

This asymmetry between tibial and femoral fixation responses demonstrates that, under an applied anterior tibial load, it originates at the tibia and propagates through the graft toward the femoral anchor. The tibial fixation, being proximal to the load application site, absorbs the primary reactive component of that force and is therefore highly sensitive to changes in graft compliance [69]. Stiffer grafts resist deformation more effectively, engaging their tibial anchor more forcefully under the same applied displacement [52, 73]. The femoral fixation, conversely, operates further along the mechanical chain and seems to appear largely decoupled from graft stiffness variability under this specific loading mode, remaining almost constant regardless of constituent material properties [52]. This finding suggests that, at least under standardized anterior drawer conditions, the tibial fixation represents the mechanically critical interface in terms of stiffness dependent load sensitivity, while the femoral anchor provides a comparatively stable mechanical boundary condition. This observation is consistent with both the discussion above about the stress distribution of the joint and the results reported by Yao et al. [69], who similarly identify the tibial tunnel aperture as a region of elevated mechanical demand under anterior tibial loading. Therefore, evaluating only anterior tibial translation, the critical point to consider in pre-surgical design and preparation is tibial site fixation.

However, it is important to note that this conclusion is specific to the loading scenario simulated. Extrapolation is not possible to other physiologically relevant conditions, such as combined rotational loading, deep knee flexion or dynamic impact. In those, the femoral fixation may assume a more prominent mechanical role, so these findings should not be consider beyond the scope of the present model.

The free body force demonstrates how much of the applied load is effectively transferred through the graft and how much is redistributed over the surrounding structures [53]. All three values remain below the applied 134 N, confirming that a portion of the anterior tibial load is, in fact, supported by adjoining anatomic components, namely the articular cartilages and menisci, rather than being entirely borne by the graft alone. This is physiologically consistent with the load-sharing behavior of the intact knee, where multiple passive and active structures contribute to restraining anterior tibial translation [53].

Expressed as a percentage of the applied load, results show that the BTBP graft carries approximately 98,1% of the total force, the QT around 85,2% and the HT only 68,4%. This gradient reveals a clear positive correlation between graft stiffness and load uptake efficiency. Stiffer constructs engage more rapidly under deformation and, therefore, assume a proportionally greater share of the applied anterior force [52, 54]. The substantially lower load transfer in the HT configuration indicates that, due to its greater compliance, the graft undergoes more deformation before reaching full mechanical engagement, allowing more of the applied force to be redistributed peripherally [73]. While this redistribution may reduce peak graft stress, as discussed before, it simultaneously increases the mechanical demand on surrounding structures, a consideration with potential implications for long term joint health [34, 69].

Taken together, these force results consolidated the biomechanical trade-off emerging from this reconstruction analysis. The BPTB graft most effectively replicates the load-bearing function of the native ACL, supporting nearly the entirety of the applied force and minimising anterior tibial displacement. However, this mechanical efficiency comes at the cost of elevated tibial fixation forces and higher intra-graft stress at the femoral exit. Conversely, the HT distributes load more broadly across the joint but at the expense of reduced stabilising capacity. The QT occupies an intermediate position across all evaluated parameters, suggesting a more balanced biomechanical profile between stability and fixation demand.

4.5 Global Considerations: Native vs. Reconstruction Scenarios

The results presented across Sections 4.1 through 4.4 collectively establish a coherent biomechanical picture of both the native knee under varying ligament properties and the reconstructed joint under distinct graft configurations.

Across all simulated scenarios, whether in native or reconstruction conditions, ligament stiffness consistently emerged as the primary determinant of anterior tibial displacement. The established inverse relationship between stiffness and translation laxity is consistent with both the fundamental constitutive behavior described by Hooke's Law for axial deformation and is broadly corroborated by computational studies under comparable conditions [52, 54]. The trend held regardless geometric configuration, considering a native complex or a simplified cylindrical construct. Quantitatively, however, the transition from native to reconstructed conditions introduced a marked amplification of anterior tibial displacement. This substantial difference cannot be attributed to stiffness, given that the Young's Modulus of BPTB is higher than that of the native conditions, and yet producing a far greater displacement. In addition to the previously mentioned reasons in the beginning of Section 4.1, this apparent paradox is explained by the simultaneous geometric transition from the complex native morphology to a cylindrical construct anchored within bone tunnels, which introduces a fundamentally different load path and fixation kinematics. In the native configuration, the ligament inserts into the bone footprints with a large and smooth contact surface. In the reconstructed model, the graft is suspended within tunnels and anchored only at their terminal boundaries, which, particularly given the angular transitions at the tunnel apertures, introduces additional compliance into the construct. This observation is consistent with the findings of Peña et al. [52] and Wan et al. [73], who note that the global stiffness of the graft-fixation-bone complex, rather than the intrinsic material stiffness of the graft alone, governs joint kinematic response.

In the native ACL, stress and strain concentration profiles underscored the variable native CSA not just as a merely morphological curiosity but also as a functionally significant structural feature, because the internal demand of the ligament was consistent with its narrowest zone. In the reconstructed models, the internal stress field reorganizes substantially. Because the cylindrical graft maintains a constant cross-section throughout its intra-articular segment, there is no geometric singularity analogous to the native mid-substance narrowing. As a result, the dominant stress concentrations migrate to the tunnel apertures, specifically to the anterior face of the femoral tunnel exit and the posterior face of the tibial tunnel entrance, where abrupt angular transitions impose localized bending and shear demands on the graft tissue. This spatial redistribution is consistent with the finite element literature [69, 72, 73] and has direct clinical implications, as it identifies the tunnel apertures, and not the mid-substance of the graft, as the primary sites of structural vulnerability under anterior loading. These are precisely the locations where graft abrasion and tunnel widening are most frequently reported clinically [34, 69].

The opposing trends observed between ligament or intra-graft stress and bone insertions or bone-interface stress across the scenarios tested represent a fundamental biomechanical trade-off. Stiffer tissues absorb a greater share of applied load internally, concentrating stress within itself, and, for the reconstruction environment, generating higher reactive forces at the tibial anchor, while more compliant materials distribute a larger proportion of the load to the surrounding peripheral joint structures, reducing intra-graft stress at the cost of elevated interface stress and reduced stabilizing capacity [69]. The QT occupies a consistent intermediate position across all evaluated parameters, anterior tibial displacement, intra-graft and interface stress, load uptake efficiency, and fixation forces, suggesting a more balanced biomechanical profile between the two extremes given by BPTB and HT.

Stiffer grafts, such as the BPTB, absorb a greater share of the applied load internally, concentrating stress within the graft tissue at the femoral exit, while simultaneously generating higher reactive forces at the tibial anchor. More compliant grafts, such as the HT, distribute a larger proportion of the load to the surrounding bone matrix and peripheral joint structures, reducing intra-graft stress at the cost of elevated interface stress and reduced stabilizing capacity. The QT occupies a consistent intermediate position across all evaluated parameters, since anterior tibial displacement, intra-graft and interface stress, load uptake efficiency, until fixation forces, suggesting a more balanced biomechanical profile between the two extremes given by BPTB and HT.

The transition from native ligament to surgical graft introduces a fundamental reorganization of how load is distributed within the joint. In the native ACL, the resultant forces at the femoral and tibial insertions were of comparable magnitude and varied non-monotonically with stiffness, suggesting a near-balanced load-sharing between the two footprints under the simulated anterior drawer. In the reconstructed configurations, this balance is broken: the tibial fixation force becomes the dominant reactive site, varying directly and substantially with graft stiffness, while the femoral fixation force remains nearly invariant across all three graft types (less than 6% variation). This asymmetry reflects the altered mechanical chain introduced by the tunnel-anchored construct, where the tibial fixation is proximal to the load source and absorbs the primary reactive component, a pattern absent in the native condition and directly attributable to the geometric and fixation transition imposed by surgery [69]. Load uptake efficiency further illustrates this divergence. In the native joint, the ACL operates as part of an integrated passive restraint system, with load naturally distributed across insertion surfaces and surrounding structures. In the reconstructed models, the proportion of the applied 134 N effectively transferred through the graft body ranged from 98% (BPTB) to 68% (HT), with the remainder redistributed to Other articular constituents. The fact that the more compliant HT transfers nearly a third of the anterior load to peripheral structures represents a meaningful deviation from native joint mechanics, with potential implications for long-term cartilage and meniscal health that fall outside the scope of this static model.

In the native ACL, strain concentration was governed by the ligament's variable cross-sectional geometry, consistently localizing to the femoral insertion where the CSA is smallest. In the reconstructed models, the constant cross-section of the cylindrical graft eliminates this geometric driver, yet strain concentration does not distribute uniformly. Instead, it migrates to the femoral tunnel exit, where the abrupt angular transition between the intra-osseous and intra-articular segments imposes localized bending demand. The longitudinal strain profiles of all three grafts shared an identical qualitative morphology despite their distinct stiffness values, with the femoral peak zone concentrating between 37% and 43% of total deformation. This confirms that the dominant determinant of strain localization shifts from material geometry in the native condition to tunnel geometry in the reconstructed condition, a transition with direct surgical implications, since it places the primary site of structural vulnerability under the control of tunnel placement and orientation rather than graft selection.

Comparing native and reconstructed conditions across all evaluated parameters, no graft configuration fully replicates the mechanical behavior of the native ACL. The BPTB graft most effectively minimizes anterior tibial displacement and maximizes load uptake, replicating the stabilizing function of the native ACL most closely in kinematic terms. However, this mechanical efficiency is accompanied by the highest intra-graft stress at the femoral exit and the greatest tibial fixation forces, which may translate into elevated risk of graft fatigue failure or tibial tunnel widening over time, particularly during the ligamentization phase when graft tissue is mechanically at its weakest [29]. The HT, by contrast, allows substantially greater anterior translation and transfers more load to the surrounding joint structures, which may protect the graft tissue from peak stress but compromises immediate joint stability and places higher demands on the tibial bone-graft interface. These findings are consistent with the clinical evidence of a higher propensity for tunnel widening and persistent laxity associated with the hamstring graft [39, 45]. The QT emerges as an intermediate option that combines acceptable joint stability with moderate fixation demands, supporting its growing clinical adoption as a balanced alternative.

To formally quantify this qualitative comparison, a weighted similarity index was constructed. For each biomechanical parameter i, a proximity score S_i was defined as:

$$S_i = \frac{\min(\text{Native}_i,\ \text{Graft}_i)}{\max(\text{Native}_i,\ \text{Graft}_i)} \tag{4.1}$$

where $S_i = 1$ indicates perfect agreement with native mechanics and $S_i \to 0$ indicates maximal divergence. Weights were assigned to reflect the clinical hierarchy of failure mechanisms: fixation interface forces received the highest collective weight, $W_2 = 0,4$, split equally between femoral and tibial components, given their direct association with tunnel widening [34, 69]; intra-graft strain, $W_1 = 0,3$, and stress, $W_3 = 0,2$, followed as primary predictors of mid-substance rupture [29, 70]; and anterior tibial displacement, $W_4 = 0,1$, was weighted lowest as a global kinematic outcome rather than a failure predictor. The resulting computed scores are presented in Table 4.10.

Table 4.10: Weighted similarity index and individual parameter scores for each graft configuration.

	BPTB	**QT**	**HT**	**w**
Strain	0,518	0,304	0,167	0,3
Femoral Fixation Force	0,635	0,622	0,601	0,2
Tibial Fixation Force	0,938	0,785	0,596	0,2
Stress	0,313	0,364	0,373	0,2
Anterior Tibial Displacement	0,145	0,111	0,078	0,1
SI	**0,547**	**0,457**	**0,372**	

No graft attains an index above 0,55, and the BPTB, despite achieving the closest overall profile, still presents substantial divergence in strain and stress parameters, as seen before. These scores numerically consolidate the qualitative trends discussed throughout this chapter and provide a reproducible metric for future cross-study comparisons of graft biomechanical fidelity.

It should be noted that, although absolute displacement values obtained in this study are lower than those reported by comparable finite element models [52, 73], the qualitative trends and relative differences between scenarios remain valid and are in agreement with the literature. As affirmed by Peña et al. [52], comparative analysis conducted within a controlled and consistent modeling framework retain their validity for identifying relative biomechanical trade-offs, even when absolute values diverge from clinical measurements. The primary contribution of this study is therefore not the replication of exact clinical displacements, but the systematic comparison of stiffness effects, geometric transitions, and graft configurations within a unified and rigorously controlled finite element environment, directly addressing the gap identified in Section 2.4 regarding the absence of models that simultaneously capture the morphological distinction between the native ACL and standardized cylindrical grafts and their biomechanical consequences.

Chapter 5

Conclusion

Besides comparing the global stiffness of ACL and surgical grafts and evaluate its impact, this dissertation aimed to also consider the geometric discrepancy between the ACL's variable, non-uniform CSA and the constant, uniform cylindrical geometry assumed for conventional surgical autografts. This work systematically isolated the structural contributions of stiffness, material non-linearity, and graft geometry to the overall biomechanical response of the knee under a standardized anterior tibial load.

The analysis of the native joint confirmed that ligament stiffness governs anterior tibial displacement through a consistently inverse, though non-linear, relationship, and that the femoral insertion, corresponding to the narrowest cross-section of the modelled ACL, emerges as the principal site of stress and strain concentration. Under lax, compliant conditions, this demand is temporarily redistributed toward a secondary, contact-driven site at the femoral-cartilage interface, but this contribution diminishes as stiffness increases, leaving the femoral footprint as the single dominant structural concern across the physiological range tested.

Interestingly, while displacement, stress and strain varied monotonically with stiffness, the resultant forces transmitted at the femoral and tibial insertions did not. Both reached their lowest values under the stiffness condition reported as normal in the literature, and increased under both the lax and stiffened configurations, suggesting that the native ACL has a physiological stiffness that may represent a near-optimal compromise between ligament deformation and insertion load transfer.

The dedicated non-linear simulation served as a methodological control for this assumption, evaluating whether the linear elastic formulation adopted for all other configurations remained adequate within the deformation magnitudes generated by the applied load.

The reconstruction phase reproduced the same inverse relationship between stiffness and anterior tibial displacement, yet the absolute translation values recorded for all three grafts were consistently and substantially higher than those observed under native conditions. This apparent contradiction is not explained by stiffness, but also the geometric and model boundary conditions.

The differences in the stress and strain distributions among native and reconstruction conditions effectively substantiates the paradox identified in the literature review: matching the global stiffness of a graft to that of the native ACL, however precisely, is insufficient to reproduce its local biomechanical behavior. Thus, graft selection protocols that rely exclusively on stiffness matching criteria therefore risk overlooking a structurally significant source of divergence from native joint mechanics.

Beyond this central insight, the comparison across BPTB, HT, and QT delineated a consistent biomechanical trade-off between internal graft stress and interface loading: stiffer constructs absorb more of the applied load internally and restrain anterior tibial translation more effectively, but transfer greater reactive force to the tibial fixation site, while more compliant grafts redistribute load toward the surrounding bone and peripheral joint structures at the expense of immediate joint stability. The quadriceps tendon occupied a consistently intermediate position across every evaluated parameter, lending quantitative support to its growing clinical adoption as a balanced alternative to the historical BPTB and HT options. Taken together, these results indicate that no single graft configuration fully reproduces native ACL mechanics, and that the tunnel apertures, rather than the graft mid-substance, constitute the primary site of structural vulnerability in the reconstructed joint, independently of the graft material selected.

5.1 Limitations

Despite the good qualitative and quantitative results here obtained, several limitations of the model and inherent to the computational framework must be acknowledge.

The native ACL geometry was constructed manually within SolidWorks, guided only by the reported values of cross-sectional and insertion area values in the literature rather than by direct segmentation of medical imaging data. While this approach allowed for a controlled, parametrisable representation of the ligament's variable cross-section, it inevitably introduces a degree of geometric approximation that a patient specific image based reconstruction, derived from MRI or CT segmentation, could substantially reduce.

The model also omits the remaining primary ligaments of the knee, namely the MCL, LCL, and PCL. Their absence was partially mitigated by the kinematic constraints imposed on the tibia, specifically the restriction of axial rotation, which was designed to approximate the secondary stabilizing role these structure provide *in vivo*. Nevertheless, their exclusion limits the model's ability to capture the full interdependence between ligaments that assure joint homeostasis.

Furthermore, the loading scenario considered throughout this work was restricted to a single, standardized 134 N anterior force applied at full knee extension. The model therefore does not account for the compressive load transmitted through the joint under body weight, nor for the range of flexion angles and combined loading modes, such as rotation or sagittal plane moments, that are clinically relevant to both injury mechanisms and post-operative rehabilitation. Given that the relative tension of the AM and PL bundles, and consequently the structural demand on both the native ligament and the reconstructed graft, is known to vary substantially across the range of motion, as seen in Chapter 2, the present findings should be understood as representative of this specific loading configuration rather than of the full physiological loading spectrum.

Finally, all joint constituents, including the ACL, the grafts, the cartilages, and the menisci, were modelled using isotropic, linear elastic material properties, with the exception of the single dedicated hyperelastic scenario described in Section 3.5. This simplification fails to capture the markedly anisotropic, and fibrous microstructure of ligamentous and tendinous tissues, nor its viscoelastic, time dependent response, which are expected to influence the long-term tensioning behavior of the graft during the ligamentization process.

It is important to emphasize, however, that the absolute values obtained throughout this work, whether of displacement, stress, or strain, are not the primary contribution of this dissertation. That contribution lies in the comparative analysis of the ACLR environment, which exposes how complex it actually is and demonstrates that mechanical properties alone are not a sufficient criterion for graft selection, contributing to the ongoing clinical and computational debate on ACLR graft choice.

5.2 Future Work

Several directions for future development follow naturally from the limitations outlined above and from the broader literature reviewed in Chapter 2.

A primary avenue concerns the geometric fidelity of both the native ligament and the surgical grafts. Reconstructing the native ACL directly from segmented medical imaging data, rather than from literature derived cross-sectional values, would yield a more anatomically faithful baseline against which graft performance could be compared. In parallel, the idealized cylindrical graft geometry adopted in this work could be refined to incorporate the morphological characteristics that make graft tissues differ among them and that are already in a early stage of compilation in Chapter 2.

A second direction involves expanding the physiological scope of the loading conditions simulated. Future iterations could incorporate the remaining knee ligaments explicitly, evaluate multiple flexion angles rather than full extension alone, and introduce combined loading modes, including axial compression representative of body weight transmission and internal-external or varus-valgus moments, to assess whether the geometric paradox identified here under anterior drawer loading persists, or is amplified, under more clinically representative conditions.

Finally, replacing the isotropic linear elastic formulation with anisotropic, fibrous, and viscoelastic constitutive models for the ligamentous and tendinous tissues would allow the time dependent evolution of graft tension during ligamentization to be captured directly, rather than inferred qualitatively from the literature. Coupled with experimental or clinical validation of the model's outputs, and with the parametrization of patient-specific anatomical and material inputs, these developments would move the present model closer to a genuinely predictive, personalized pre-operative planning tool for anterior cruciate ligament reconstruction.

References

[1] *Ods • objetivos desenvolvimento sustentável • bcsd portugal*. [Online]. Available: https://ods.pt/.

[2] A. Pinheiro and A. D. Costa Pinheiro, "Lesão do ligamento cruzado anterior: Apresentação clínica, diagnóstico e tratamento," *Revista Portuguesa de Ortopedia e Traumatologia*, 2015.

[3] E. Svantesson, E. H. Senorski, K. E. Webster, and J. Karlsson, "Clinical outcomes after anterior cruciate ligament injury: Panther symposium," *Knee Surgery, Sports Traumatology, Arthroscopy*, 2020. DOI: 10.1007/S00167-020-06061-X.

[4] B. T. Samuelsen, K. E. Webster, N. R. Johnson, T. E. Hewett, and A. J. Krych, "Hamstring autograft versus patellar tendon autograft for acl reconstruction," *Clinical orthopaedics and related research*, 2017. DOI: 10.1007/S11999-017-5278-9.

[5] M. Elfekky et al., "Causes of anterior cruciate ligament reconstruction failure: A meta-analysis," *Journal of Musculoskeletal Surgery and Research*, 2022. DOI: 10.25259/JMSR_72_2022.

[6] A. Gupta et al., "Surgical techniques, outcomes, indications, and complications of simultaneous high tibial osteotomy and anterior cruciate ligament revision surgery: A systematic review.," *HSS Journal*, 2019. DOI: 10.1007/s11420-018-9630-8.

[7] E. McDermott, M. T. DeFoor, O. K. Blaber, Z. S. Aman, N. N. DePhillipo, and T. J. Dekker, "Biomechanical comparison of anterior cruciate ligament reconstruction fixation methods and implications on clinical outcomes," *Annals of Joint*, 2023. DOI: 10.21037/aoj-22-52.

[8] S. Verhagen, M. Dietvorst, E. Delvaux, M. van der Steen, and R. Janssen, "Clinical outcomes of different autografts used for acl reconstruction in skeletally immature patients," *BMC Musculoskeletal Disorders*, 2023. DOI: 10.1186/s12891-023-06749-4.

[9] C. Ashy et al., "Quadriceps tendon autograft has similar clinical outcomes for revision acl reconstruction," *Knee surgery, sports traumatology, arthroscopy*, 2023. DOI: 10.1007/S00167-023-07592-9.

[10] S. Tapasvi and A. Shekhar, "Revision acl reconstruction: Principles and practice.," *Indian journal of Orthopaedics*, 2021. DOI: 10.1007/s43465-020-00328-8.

[11] D. Mouarbes, J. Menetrey, V. Marot, L. Courtot, E. Berard, and E. Cavaignac, "Anterior cruciate ligament reconstruction: Outcomes for quadriceps tendon autograft," *American Journal of Sports Medicine*, 2019. DOI: 10.1177/0363546518825340.

[12] M. T. Banovetz, N. I. Kennedy, R. F. LaPrade, L. Engebretsen, and G. Moatshe, "Biomechanical considerations for graft choice in anterior cruciate ligament reconstruction.," *Annals of Joint*, 2023. DOI: 10.21037/aoj-22-50.

[13] K. Markatos, M. K. Kaseta, S. N. Lallos, D. S. Korres, and N. Efstathopoulos, "The anatomy of the acl and its importance in acl reconstruction," *European Journal of Orthopaedic Surgery & Traumatology*, 2012. DOI: 10.1007/S00590-012-1079-8.

[14] A. L. Nogueira and R. Matos, "Forças do ligamento cruzado anterior após reconstrução, estudo experimental," Universidade de Aveiro, Tech. Rep., 2025.

[15] J. R. R. d. Santos, "Rotura do ligamento cruzado anterior e as diferentes opções de enxerto na sua reconstrução cirúrgica medicina," Faculdade de Ciências da Saúde, Tech. Rep., 2026.

[16] C. Daniel, "Análise biomecânica da reconstrução do ligamento cruzado anterior," Instituto Politécnico de Leiria, Tech. Rep., 2026.

[17] R. L. Drake, W. Vogl, A. W. M. Mitchell, and H. Gray, *Gray's Anatomy for Students*, 3rd. Churchill Livingstone/Elsevier, 2015.

[18] C. D. Correia, "Desenvolvimento de modelo multicorpo da articulação do joelho para estudo do ligamento cruzado anterior," Universidade de Aveiro, Tech. Rep., 2024.

[19] N. L. Leong et al., "Use of ultra-high molecular weight polycaprolactone scaffolds for acl reconstruction," *Journal of Orthopaedic Research*, 2016. DOI: 10.1002/jor.23082.

[20] Teach me Anatomy, *The knee joint - articulations - movements - injuries*, 2024. Accessed: Jan. 9, 2026. [Online]. Available: https://teachmeanatomy.info/lower-limb/joints/knee-joint/.

[21] S. Kopf, V. Musahl, S. Tashman, M. Szczodry, W. Shen, and F. H. Fu, "A systematic review of the femoral origin and tibial insertion morphology," *Knee Surgery, Sports Traumatology, Arthroscopy*, 2009. DOI: 10.1007/S00167-008-0709-5.

[22] M. Fernandes, "Medida da deformação do ligamento cruzado anterior," Ph.D. dissertation, Faculdade de Engenharia da Universidade do Porto, Jul. 2013.

[23] A. C. Vieira, R. M. Guedes, and A. T. Marques, "Development of ligament tissue biodegradable devices: A review," Faculdade de Engenharia da Universidade do Porto, Tech. Rep., 2026.

[24] M. Dienst, R. T. Burks, and P. E. Greis, "Anatomy and biomechanics of the anterior cruciate ligament," *Orthopedic Clinics of North America*, vol. 33, pp. 605–620, 4 Oct. 2002, ISSN: 0030-5898. DOI: 10.1016/S0030-5898(02)00010-X. [Online]. Available: https://www.sciencedirect.com/science/article/pii/S003058980200010X?via%3Dihub.

[25] C. Kweon, E. Lederman, and A. Chhabra, "Anatomy and biomechanics of the cruciate ligaments and their surgical implications," in *The Multiple Ligament Injured Knee: A Practical Guide to Management*. Springer, 2013, pp. 17–28.

[26] J. Noronha, "Isometria na reconstrução do ligamento cruzado anterior," Ph.D. dissertation, Instituto de Ciências Biomédicas Abel Salazar da Universidade do Porto, 1999.

[27] A. M. Kiapour and M. M. Murray, "Basic science of anterior cruciate ligament injury and repair," *Bone and Joint Research*, 2014. DOI: 10.1302/2046-3758.32.2000241.

[28] G. DeMorat, P. Weinhold, T. Blackburn, S. Chudik, and W. Garrett, "Aggressive quadriceps loading can induce noncontact acl injury," *The American Journal of Sports Medicine*, 2004. DOI: 10.1177/0363546503258928.

[29] D. J. Magee, J. E. Zachazewski, W. S. Quillen, and R. C. Manske, *Pathology and intervention in musculoskeletal rehabilitation*. Saunders, 2016.

[30] H. C. Urreiztieta, D. B. Spence, C. P. Bankhead, and D. L. Richter, "Treatment strategies for concomitant ligament injury in anterior cruciate ligament-injured athletes," *Annals of Joint*, 2025. DOI: 10.21037/aoj-25-28.

[31] R. Oikawa et al., "Morphology of the patellar tendon and its insertion sites," *The Knee*, 2019. DOI: 10.1016/J.KNEE.2018.12.002.

[32] B. Shetty, S. Shetty, and P. K. Umesh, "Semitendinosus tendon morphometry as a graft - a cadaver study," *National Journal of Clinical Anatomy*, 2022. DOI: 10.4103/NJCA.NJCA_95_21.

[33] S. Latiff and O. I. Olateju, "Morphometry of the harvestable surface area of quadriceps tendon," *European Journal of Anatomy*, 2022. DOI: 10.52083/TDBN2622.

[34] E. Elango, "Graft fixation techniques in anterior cruciate ligament reconstruction – a narrative review," *Journal of Arthroscopic Surgery and Sports Medicine*, 2024. DOI: 10.25259/jassm_12_2023.

[35] A. Ramos, C. Anacleto, and J. A. Simões, "Insights from a computational model of anterior cruciate ligament reconstruction," *Results in Engineering*, 2025. DOI: 10.1016/J.RINENG.2025.106215.

[36] J. T. Bencardino, J. Beltran, M. I. Feldman, and D. J. Rose, "Mr imaging of complications of acl graft reconstruction," *Radiographics*, 2009. DOI: 10.1148/RG.297095036.

[37] D. C. Meyer, M. Stalder, P. P. Koch, J. G. Snedeker, and M. Farshad, "Contact pressure on acl hamstring grafts in the bone tunnel," *The Knee*, 2012. DOI: 10.1016/J.KNEE.2011.11.005.

[38] Y. Xiao et al., "Dual fluoroscopic imaging and ct-based finite element modelling," *International Journal of Computer Assisted Radiology and Surgery*, 2021. DOI: 10.1007/S11548-021-02307-2.

[39] M. Ostojic et al., "Graft selection in anterior cruciate ligament reconstruction: A comprehensive review of current trends," *Medicina (Lithuania)*, 2024. DOI: 10.3390/medicina60122090.

[40] X. Zheng et al., "Clinical outcomes and second-look arthroscopic findings of anterior cruciate ligament reconstruction," *Journal of Orthopaedic Surgery and Research*, 2019. DOI: 10.1186/s13018-019-1439-8.

[41] J. Baawa-Ameyaw, R. Plastow, F. A. Begum, B. Kayani, H. Jeddy, and F. Haddad, "Current concepts in graft selection for anterior cruciate ligament reconstruction," *EFORT Open Reviews*, 2021. DOI: 10.1302/2058-5241.6.210023.

[42] D. I., *5 principais enxertos: Ligamento cruzado anterior (lca)*, 2024. Accessed: Jan. 12, 2026. [Online]. Available: https://iberedatti.com.br/blog/enxertos-para-o-ligamento-cruzado-anterior/.

[43] J. S. Ribeiro and A. C. Donda, "Reconstrução de ligamento cruzado anterior reconstruction of anterior cross ligament," *Revista Científica Multidisciplinar*, 2026.

[44] J. D. Placzek and D. A. Boyce, *Orthopaedic physical therapy secrets*. Elsevier, 2017.

[45] P. Zalewska, A. Góralczyk, T. Guszczyn, K. Hermanowicz, and S. Piszczatowski, "Biomechanics of periarticular knee muscles after acl surgery in young patients," *Acta of Bioengineering and Biomechanics*, 2025. DOI: 10.37190/abb-02564-2024-02.

[46] J.-R. H. Smith et al., "Five-strand hamstring autografts for anterior cruciate ligament reconstruction," *Orthopaedic Journal of Sports Medicine*, 2019. DOI: 10.1177/2325967119826094.

[47] G. Vinagre et al., "Hamstring graft preparation techniques for acl reconstruction," *Arthroscopy Techniques*, 2017. DOI: 10.1016/j.eats.2017.08.031.

[48] M. Dietvorst, M. C. M. van der Steen, M. van den Besselaar, and R. P. Janssen, "Height is a predictor of hamstring tendon length and acl graft characteristics in adolescents," *BMC Musculoskeletal Disorders*, vol. 24, 2023. DOI: 10.1186/s12891-023-06705-2.

[49] W. M. Wang, X. J. Ma, S. B. Huang, L. B. Ren, and Y. P. Liu, "A comparative study of effect of autograft compared with allograft anterior cruciate ligament reconstruction," *Bioscience Reports*, 2017. DOI: 10.1042/BSR20160533.

[50] S. J. Rabuck, V. Musahl, F. H. Fu, and R. V. West, "Anatomic anterior cruciate ligament reconstruction with quadriceps tendon autograft," *Clinics in Sports Medicine*, 2013. DOI: 10.1016/J.CSM.2012.08.014.

[51] J. W. Xerogeanes, "Quadriceps tendon graft: The graft of the future!" *Arthroscopy*, 2019. DOI: 10.1016/J.ARTHRO.2019.01.011.

[52] E. Peña, M. A. Martínez, B. Calvo, D. Palanca, and M. Doblaré, "A finite element simulation of the effect of graft stiffness and graft tensioning," *Clinical Biomechanics*, 2005. DOI: 10.1016/J.CLINBIOMECH.2004.07.014.

[53] L. Benos, D. Stanev, L. Spyrou, K. Moustakas, and D. E. Tsaopoulos, "A review on finite element modeling and simulation of acl reconstruction," *Frontiers in Bioengineering and Biotechnology*, 2020. DOI: 10.3389/FBIOE.2020.00967.

[54] A. L. Kapandji, *Fisiologia articular, volume 2 : esquemas comentados de mecânica humana*, Tradução 5ª. Rio de Janeiro: Guanabara Koogan, 2000.

[55] insideortho, *Lesão do ligamento cruzado anterior – insideortho*, 2024. Accessed: Jan. 13, 2026. [Online]. Available: https://insideortho.org/pt/lesao-ligamento-cruzado-anterior/.

[56] S. B. Wahed et al., "Functional ultra-high molecular weight polyethylene composites for ligament reconstructions," *Polymers*, 2022. DOI: 10.3390/POLYM14112189.

[57] M. Ferretti Filho, F. Quercia Allen, and C. P. Helito, "Avaliação da rigidez do ligamento cruzado anterior e dos enxertos," *Acta Ortopédica Brasileira*, 2002.

[58] S. J. Breda, A. van der Vlist, R. J. de Vos, G. P. Krestin, and E. H. G. Oei, "The association between patellar tendon stiffness measured with shear-wave elastography," *European Radiology*, 2020. DOI: 10.1007/S00330-020-06952-0.

[59] B. T. Haraldsson, P. Aagaard, M. Krogsgaard, T. Alkjaer, M. Kjaer, and S. P. Magnusson, "Region-specific mechanical properties of the human patella tendon," *Journal of Applied Physiology*, 2005. DOI: 10.1152/JAPPLPHYSIOL.00482.2004.

[60] R. B. Svensson et al., "Mechanical properties of human patellar tendon at hierarchical levels," *Journal of Applied Physiology*, 2012. DOI: 10.1152/JAPPLPHYSIOL.01172.2011.

[61] O. Basso, D. P. Johnson, and A. A. Amis, "The anatomy of the patellar tendon," *Knee surgery, sports traumatology, arthroscopy*, 2001. DOI: 10.1007/S001670000133.

[62] S. Latiff and O. I. Olateju, "Morphometry of the patellar tendon using a simple tracing method," *Anatomy & Cell Biology*, 2023. DOI: 10.5115/ACB.22.169.

[63] J. H. Yoo, S. R. Yi, and J. H. Kim, "The geometry of patella and patellar tendon measured on knee mri," *Surg Radiol Anat*, 2007. DOI: 10.1007/s00276-007-0261-x.

[64] T. Education, *Anatomy - patellartendinopathy*, 2024. [Online]. Available: https://patellartendinopathy.trekeducation.org/anatomy/.

[65] D. W. Dziedzic, U. Bogacka, I. Komarniţki, and B. Ciszek, "Anatomy and morphometry of the distal gracilis muscle tendon," *Folia Morphologica (Poland)*, 2018. DOI: 10.5603/FM.a2017.0069.

[66] J. Zhu, X. Zhang, Y. Ma, C. Zhou, and Y. Ao, "Ultrastructural and morphological characteristics of human acl," *Anatomical Record*, 2012. DOI: 10.1002/AR.22527.

[67] S. Di Paolo, A. Grassi, G. A. Lucidi, L. Macchiarola, G. Dal Fabbro, and S. Zaffagnini, "Biomechanics of the lateral meniscus," *Annals of joint*, 2022. DOI: 10.21037/aoj-20-123.

[68] S. Klich et al., "Quadriceps and patellar tendon thickness and stiffness in elite track cyclists," *Frontiers in Physiology*, 2020. DOI: 10.3389/FPHYS.2020.607208.

[69] J. Yao et al., "Deterioration of stress distribution due to tunnel creation," *Annals of biomedical engineering*, 2012. DOI: 10.1007/S10439-012-0517-4.

[70] S. F. Siemoneit et al., "Histomorphological changes in autologous anterior cruciate ligament graft failure show predominantly inflammatory reactions, fissure defects and osteonecrosis," *Journal of Experimental Orthopaedics*, vol. 12, 4 Oct. 2025, ISSN: 2197-1153. DOI: 10.1002/JEO2.70545. [Online]. Available: https://pubmed.ncbi.nlm.nih.gov/41323544/.

[71] J. P. van der List, D. N. Mintz, and G. S. DiFelice, "The location of anterior cruciate ligament tears: A prevalence study using magnetic resonance imaging," *Orthopaedic Journal of SportsMmedicine*, vol. 5, 6 Jun. 2017, ISSN: 2325-9671. DOI: 10.1177/2325967117709966. [Online]. Available: https://pubmed.ncbi.nlm.nih.gov/28680889/.

[72] J. Zhu, W. Zhu, and Q. Zhao, "Computational modelling of the graft-tunnel interaction," *Biomedizinische Technik*, 2023. DOI: 10.1515/BMT-2022-0136.

[73] C. Wan, Z. Hao, Z. Li, and J. Lin, "Finite element simulations of different hamstring tendon graft lengths," *Medical & Biological Engineering & Computing*, 2017. DOI: 10.1007/S11517-017-1637-7.

[74] X. Chen et al., "Finite element analysis of anterior cruciate ligament reconstruction techniques," *Frontiers in Bioengineering and Biotechnology*, 2024. DOI: 10.3389/FBIOE.2024.1438839.

[75] F. Amirouche, G. F. Solitro, B. Z. Gligor, M. Hutchinson, and J. Koh, "Investigating the effect of autograft diameter for quadriceps and patellar tendons," *Frontiers in Surgery*, 2023. DOI: 10.3389/FSURG.2023.1122379/FULL.

[76] L. Wang et al., “Anterior cruciate ligament reconstruction and cartilage contact forces–a 3d computational simulation,” *Clinical biomechanics (Bristol, Avon)*, vol. 30, pp. 1175–1180, 10 Dec. 2015. [Online]. Available: https://pubmed.ncbi.nlm.nih.gov/26320976/.

[77] I. Mediavilla, M. Aramberri, G. Tiso, E. Margalet, and F. Abat, “Artroscopia y cirugía articular basic sciences in reconstruction of the anterior cruciate ligament with the ischiotibial tendons (a narrative review),” *Revista Española de Artroscopia y Cirugía Articular*, vol. 30, pp. 32–42, 1 2023, ISSN: 2443-9754. DOI: 10.24129/j.reacae.30178.fs2207013. [Online]. Available: https://doi.org/10.24129/j.reacae.30178.fs2207013.

[78] D. Fernandes, “Finite element analysis of the acl-deficient knee,” Ph.D. dissertation, Instituto Superior Técnico, Dec. 2014.

[79] R. Cheng, H. Wang, Z. Jiang, D. Dimitriou, C. K. Cheng, and T. Y. Tsai, “The femoral tunnel drilling angle at 45° coronal and 45° sagittal provided the lowest peak stress and strain on the bone tunnels and anterior cruciate ligament graft,” *Frontiers in Bioengineering and Biotechnology*, vol. 9, Nov. 2021, ISSN: 2296-4185. DOI: 10.3389/FBIOE.2021.797389. [Online]. Available: https://pubmed.ncbi.nlm.nih.gov/34900975/.

[80] X. Zhang, G. Jiang, C. Wu, and S. L. Woo, “A subject-specific finite element model of the anterior cruciate ligament,” *Annual International Conference of the IEEE Engineering in Medicine and Biology Society. IEEE Engineering in Medicine and Biology Society. Annual International Conference*, vol. 2008, pp. 891–894, 2008, ISSN: 2375-7477. DOI: 10.1109/IEMBS.2008.4649297. [Online]. Available: https://pubmed.ncbi.nlm.nih.gov/19162800/.

[81] J. C. Noronha and J. P. Oliveira, “Inside-out tibial tunnel drilling technique for all-inside acl reconstruction,” *Arthroscopy Techniques*, 2018. DOI: 10.1016/J.EATS.2017.10.008.